Geochemistry Geophysics Geosystems G3

Article
Volume 11
11 June 2010
Q0AA07, doi:10.1029/2010GC003069
ISSN: 1525-2027

Published by AGU and the Geochemical Society

High-resolution rock magnetic cyclostratigraphy in an Eocene flysch, Spanish Pyrenees

K. P. Kodama, D. J. Anastasio, and M. L. Newton
Department of Earth and Environmental Sciences, Lehigh University, 31 Williams Drive, Bethlehem, Pennsylvania 18015-3188, USA (kpk0@lehigh.edu)

J. M. Pares
Department of Geological Sciences, University of Michigan, 2534 C.C. Little Building, 1100 North University Avenue, Ann Arbor, Michigan 48109-1005, USA

Now at Centro Nacional de Investigación sobre Evolución Humana, Avenida de la Paz 28, E-09004 Burgos, Spain

L. A. Hinnov
Department of Earth and Planetary Sciences, Johns Hopkins University, 301 Olin Hall, 3400 North Charles Street, Baltimore, Maryland 21218, USA

[1] A rock magnetic cyclostratigraphy, based on anhysteretic remanent magnetization (ARM) intensity variations, was developed for the Eocene Arguis Formation in the Spanish Pyrenees. The Arguis Formation was sampled for ARM cyclostratigraphy, rock magnetic, and paleomagnetic analyses. Rock magnetic measurements indicate that the dominant magnetic mineral controlling the ARM cyclostratigraphy is depositional magnetite. Using thermal demagnetization, a detailed magnetostratigraphy was developed for the Arguis to provide an absolute time framework for the ARM cyclostratigraphy. The magnetostratigraphy is carried by a combination of depositional magnetite and secondary iron sulfides. Spectral analysis of the magnetostratigraphically scaled ARM time series reveals the presence of significant Milankovitch frequencies including eccentricity, obliquity, and precession. The ARM time series was tuned to the orbital eccentricity model for the Eocene. Coherency analysis indicates that the eccentricity-tuned ARM is in phase with October–November insolation for this site's paleolatitude. Varying amounts of terrigenous input delivered by a fluvial source at orbital time scales, during the rainy season, and diluted by a relatively constant input of marine carbonate is the most likely explanation for the cyclicity of the ARM record. The absolute age resolution of the ARM chronostratigraphy is 1% or less based on an age offset with the reference chronology that was used for the Eocene. The offset in age between the two chronologies may be due, in part, to the uncertainty in the chron ages for this part of the Eocene. The relative age resolution within the ARM chronostratigraphy is much better.

Components: 11,800 words, 13 figures, 2 tables.

Keywords: cyclostratigraphy; magnetostratigraphy; rock magnetics; Late Eocene; ARM; paleoclimate.

Index Terms: 4910 Paleoceanography: Astronomical forcing; 1520 Geomagnetism and Paleomagnetism: Magnetostratigraphy; 1540 Geomagnetism and Paleomagnetism: Rock and mineral magnetism.

Received 1 February 2010; **Revised** 19 April 2010; **Accepted** 29 April 2010; **Published** 11 June 2010.

Kodama, K. P., D. J. Anastasio, M. L. Newton, J. M. Pares, and L. A. Hinnov (2010), High-resolution rock magnetic cyclostratigraphy in an Eocene flysch, Spanish Pyrenees, *Geochem. Geophys. Geosyst.*, *11*, Q0AA07, doi:10.1029/2010GC003069.

Theme: EarthTime: Advances in Geochronological Technique
Guest Editors: D. Condon, G. Gehrels, M. Heizler, and F. Hilgen

1. Introduction

[2] Cyclostratigraphy includes the study of astronomically forced climate cycles recorded in sediments and sedimentary rocks. The climate cycles occur in a wide array of depositional environments [*Berger et al.*, 1984; *de Boer and Smith*, 1994; *House and Gale*, 1995; *Shackleton et al.*, 1999a, 1999b; *Pälike et al.*, 2001; *Kruiver et al.*, 2002; *d'Argenio et al.*, 2004; *Berger et al.*, 2005; *Olsen and Whiteside*, 2008; *Pickering and Bayliss*, 2009]. When calibrated to accurate models of Earth's orbital motions, cyclostratigraphy provides a high-resolution metronome with a precision, accuracy and continuity that outperforms modern radioisotope geochronology, magnetostratigraphy, or biostratigraphy. The time resolution of orbitally forced cyclostratigraphy ranges from 0.02 to 0.1 Myr, reflecting the periodicity of the forcing parameters, i.e., the 18–23 kyr precession index, ~40 kyr obliquity, and 95–128 kyr and 405 kyr orbital eccentricity [*Laskar et al.*, 2004].

[3] Proxies commonly used to recover cyclostratigraphy from sedimentary strata are often derived from geochemistry (e.g., carbon and oxygen stable isotopes, total organic carbon), lithology (grain size, color, carbonate content, biogenic silica), facies (relative water depth), paleontology (relative taxon abundance, foram coiling) (summaries by *Hinnov* [2000] and *Hinnov* [2004]). Orbitally forced sedimentary cycles have also been recovered from magnetic susceptibility (χ) [*Bloemendal et al.*, 1988; *Mayer and Appel*, 1999; *Shackleton et al.*, 1999b; *Ellwood et al.*, 2007]. However, low-field magnetic susceptibility is a bulk measurement of the concentration of all ferromagnetic, diamagnetic, and paramagnetic minerals in a sample, making climate-related interpretation of susceptibility records complicated. Alternatively, anhysteretic remanent magnetization (ARM) measures the concentration of low-coercivity ferromagnetic minerals only, data amenable to a less ambiguous interpretation. The identification of astronomically forced climate cycles in the rock record requires samples closely spaced in time (<5 kyr) collected over a long time period (>2 Myr), necessitating the analysis of numerous samples. Because ARM measurements do not require oriented samples, are nondestructive, and are relatively quick, ARM is an ideal tool for developing a cyclostratigraphy. *Latta et al.* [2006] successfully recovered Milankovitch periodicities from ARM records in Cretaceous carbonates from northeastern Mexico. Latta et al. argued that astronomically forced global aridity caused eolian magnetite concentrations to vary at precession frequencies in the carbonates.

[4] In this study we develop a methodology to recover Milankovitch cycles from an ARM record in Eocene marine deltaic rocks deposited in the Jaca piggyback basin of the Spanish Pyrenees. We also refine *Hogan and Burbank*'s [1996] magnetostratigraphy of the Arguis Formation to provide tighter absolute time constraints for the ARM chronostratigraphy. To remove the effect of sedimentation rate changes that can cause distortion of the climate time series we tune our ARM record to Earth's orbital eccentricity model for the Eocene [*Laskar et al.*, 2004]. Coherency analysis comparing the tuned series and insolation provides information relevant to the encoding of the ARM cyclostratigraphic signal.

[5] This study demonstrates the power of using ARM as a robust and objective measure of orbitally forced climate cycles in clastic marine sedimentary rocks that otherwise have only subtle variations in lithology and sedimentary facies as a record of cyclostratigraphy. In combination with the refined magnetostratigraphy reported here, we establish depositional ages with 200–400 kyr resolution, and relative ages within the section with a 50 kyr resolution.

2. Geologic Setting

2.1. Spanish Pyrenees and the Jaca Basin

[6] The Pyrenees are a doubly vergent, east–west trending Cretaceous-Tertiary orogen along the border between the Iberian block and the Eurasian Plate (Figure 1) [*Roest and Srivastava*, 1991]. The orogen

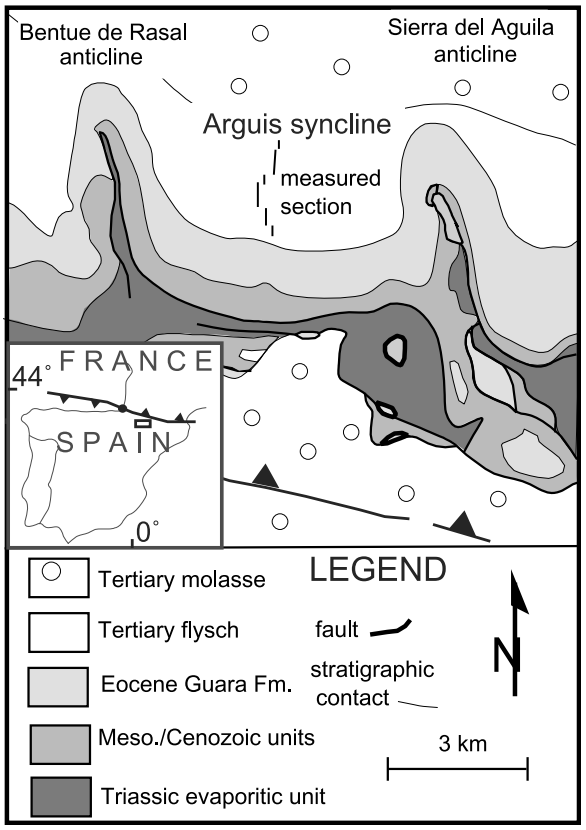

Figure 1. Location map of a portion of the External Sierra and the southern margin of the Jaca basin. The section studied is located in the Arguis syncline, adjacent to the Pico (Sierra) del Aguilla anticline to the east [after *Anastasio and Holl*, 2001]. The Tertiary flysch unit represents both the Arguis Formation and the Belsue-Atares Formation.

is relatively young, with deformation and synorogenic deposition continuing into the Miocene (~18 Ma) [*dePaor and Anastasio*, 1987; *Meigs*, 1997]. An axial zone of basement-cored thrusts characterizes the orogenic hinterland, with outward vergent thrust belts to the north and the south. The Spanish Pyrenees consist of the thrust sheets and transported syntectonic basins to the south of the axial zone and the External Sierra, a series of foothills along the southern thrust front [*Puigdefabregas*, 1975; *Labaume et al.*, 1985; *Anastasio*, 1992]. The Jaca basin is a structurally partitioned piggyback basin located in the southern Pyrenees. Transport of the Jaca basin and the foreland migration of the External Sierra thrust front occurred on a thrust fault with a décollement in Triassic evaporitic strata. The Jaca basin records deposition from the middle Eocene through the Oligocene [*Puigdefabregas*, 1975; *Millan et al.*, 1994; *Hogan and Burbank*, 1996]. Paleogene clastic rocks in the Jaca basin were deposited from east to

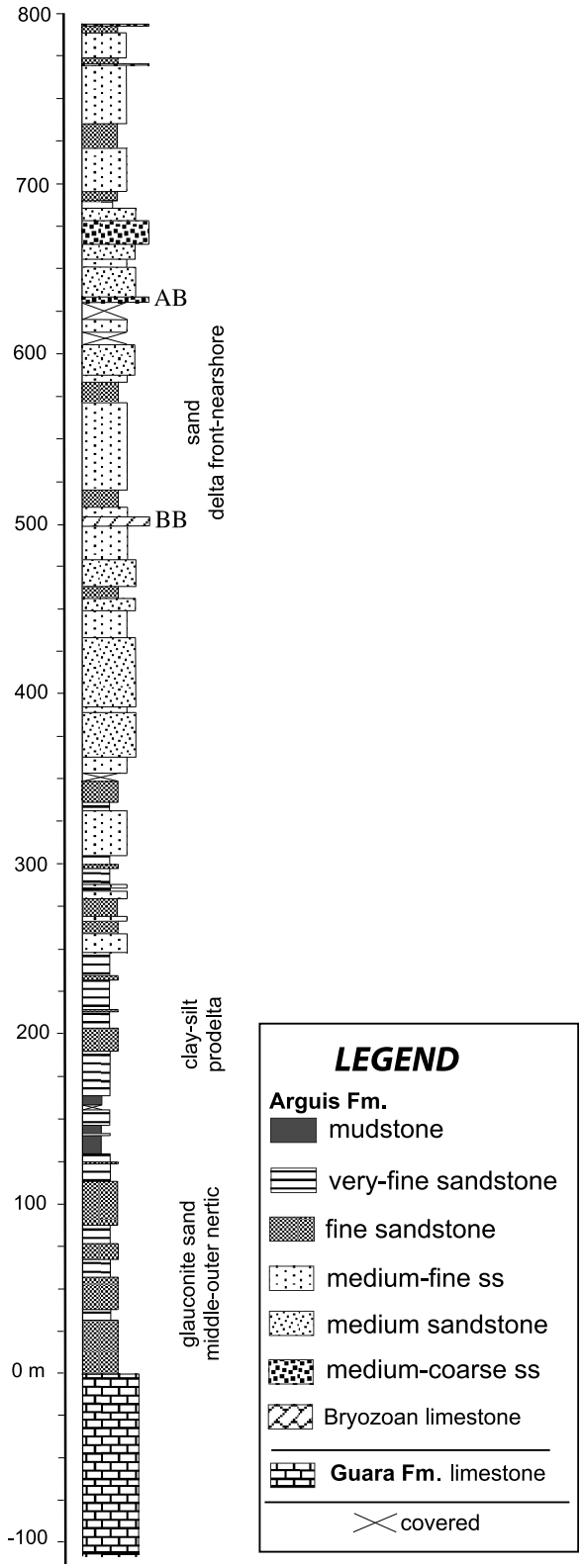

Figure 2. Stratigraphic column for the Arguis Formation in the Arguis syncline. Horizontal scales based on grain size and lithology. Stratigraphic distance in meters (m). AB, Arguis Bed; BB, Bryozoan Bed.

west, and represent a marine to continental facies transition [*Puigdefabregas*, 1975; *Mutti et al.*, 1988; *Castelltort et al.*, 2003].

2.2. Arguis Formation in the Arguis Syncline

[7] The Arguis Formation is the target of this cyclostratigraphic and magnetostratigraphic study. It is a Tertiary flysch unit composed of beds of marly siltstones, fine-grained sandstones, medium-grained bioturbated sandstones, coarse-grained sandstones, and rare interbedded limestones (Figure 2). The depositional environment is characterized by a mixed siliciclastic/carbonate setting in which fluvial-, storm-, and tidal-influenced sedimentation dominated, generally trending toward more shallow and coarse facies up section [*Castelltort et al.*, 2003]. The lower boundary of the Arguis Formation is marked by a contact with the marine carbonates of the Guara Formation. The upper boundary of the Arguis is a gradational contact with the coarse-grained shallow marine deltaic sandstone of the Belsue-Atares Formation [*Puigdefabregas*, 1975; *Millan et al.*, 1994]. A latest Lutitian to early Priabonian age of the Arguis Formation is supported by multispecies biostratigraphy [*Canudo*, 1990; *Canudo et al.*, 1991] and magnetostratigraphy [*Hogan*, 1993; *Pueyo et al.*, 2002; *Pares et al.*, 2006]. Biostratigraphy suggests that the Arguis Formation spans from nanoplankton (NP) zone NP16 to NP17 and planktonic foraminifera (P) zone P12 to P15 [*Canudo et al.*, 1991].

[8] The Arguis Formation is greater than 800 m thick in the Arguis syncline (Figure 1) [*Puigdefabregas*, 1975; *Millan et al.*, 1994; *Castelltort et al.*, 2003; *Hogan*, 1993; *Pueyo et al.*, 2002; *Newton*, 2006]. The ARM cyclostratigraphy reported here was developed for nearly all of the Arguis Formation (Figure 2). Grain size, bioturbation, fossil composition, and bed thickness were assessed every ~10 cm. The base of the Arguis section consists of fine blue-gray marls and several prominent glauconitic sand beds, which represent a diastem or hiatus in deposition [*Puigdefabregas*, 1975]. The depositional environment of the Arguis Formation begins as 120 m middle-outer neritic deltaic slope deposition formed entirely below wave base [*Castelltort et al.*, 2003]. Deposition was slow resulting in a condensed section. The basal unit is overlain by 385 m of prograding prodelta silt and clay deposited at a higher rate in the Arguis syncline. Bioturbation and fossil content increase up section where the sequence is capped by a bryozoan limestone bed two to 12 m thick (sequence 2 of *Millan et al.* [1994]). The sequence includes graded beds interpreted to be storm deposits, which formed on a low-angle slope [*Millan et al.*, 1994]. The uppermost Arguis Formation consists of >500 m delta front sand, mouth bar, and tidal facies deposited at an even higher rate during delta retrogradation. Overall the Arguis Formation represents a large-scale prograding/retrograding deltaic sequence deposited from east to west, burying the active Sierra del Aguila anticline. The Arguis Formation is overlain by the Belsue-Atarés Formation, that represents delta plain environments and finally the postfolding Compodarbe Formation, which represents Oligocene-Miocene aged fluvial molasse.

[9] Three suites of samples were collected from the Arguis Formation for this study, one set was collected to analyze rock magnetic cyclostratigraphy, a second set was collected to conduct rock magnetic tests on each distinct lithology found throughout the Arguis type section, and the third suite of oriented samples was collected to refine the magnetostratigraphy previously reported by *Hogan and Burbank* [1996].

3. Methods

3.1. Rock Magnetic Analysis

[10] Samples for rock magnetic analysis were collected from five representative lithologies within the section; mudstone (<4.0 ϕ), very fine grained sandstone (4.0–3.5 ϕ), fine-grained sandstone (3.5–3.0 ϕ), medium-grained, bioturbated sandstone (3.0–2.0 ϕ), and coarse-grained sandstone (2.0–1.5 ϕ). Nine to thirteen oriented cores were drilled from each site, generating between 1 and 3 samples per core. Samples from each site were used to identify (1) the magnetic mineralogy contributing to the magnetostratigraphy based on coercivity and unblocking temperature from thermal demagnetization of three orthogonal components of isothermal remanent magnetization (IRM) [*Lowrie*, 1990], (2) the magnetic mineralogy contributing to the ARM cyclostratigraphy by thermal demagnetization of two orthogonal partial ARMs (pARMs), and (3) the relative contributions to remanence by different coercivity phases using IRM acquisition modeling [*Kruiver et al.*, 2001].

[11] IRMs were applied in an ASC Scientific IM-10-30 impulse magnetizer in three orthogonal directions to three samples from each of three sites. A field of 1.2 T was applied along the *x* axis, 0.6 T

Table 1. Arguis Formation Chron Boundary Position and Age

Chron Boundary	Stratigraphic Position (m)	Age[a] (kyr BP)
C18r-C18n.2n	39.6	39,464
C18n.2n-C18n.1r	75.4	39,041
C18n.1r-C18n.1n	86.075	38,975
C18n.1n-C17r	321.15	38,032
C17r-C17n.3n	370.25	37,771
C17n.3n-C17n.2r	468.55	37,610
C17n.2r-C17n.2n	487.65	37,549
C17n.2n-C17n.1r	515.65	37,345
C17n.1r-C17n.1n	563.70	37,235
C17n.1n-C16r	707.0	36,512

[a]*Gradstein et al.* [2004].

was then applied along the *y* axis, and finally 0.1 T was applied along the z axis. The pARMs were applied with a modified Schonstedt GSD-5 AC demagnetizer. The DC field was 97 μT and the pARMs were applied in a 100–60 mT alternating field window along the *x* axis and a 30–0 mT alternating field window along the *y* axis. These fields were chosen based on the IRM acquisition modeling. Following the applications of the IRMs and pARMs, each sample was thermally demagnetized in 50°C steps from 100°C to 600°C [*Lowrie*, 1990]. Thermal demagnetization was performed in an ASC Scientific TD-48 thermal specimen demagnetizer. Remanence was measured in a 2G Enterprises, Inc. 755R superconducting magnetometer.

[12] Detailed IRM acquisition experiments were conducted in 26 steps in the impulse magnetizer. The samples had not been exposed previously to any strong magnetic fields. Fields between 4 and 207 mT were applied in 11 steps in a 25 mm diameter coil while fields between 254 mT and 5005 mT were applied in 15 steps in a 12 mm diameter coil. Steps were chosen to be as uniform as possible in a log scale; however, the impulse magnetizer makes close spacing of steps at fields less than 50 mT difficult. Coercivity components were forward modeled using *Kruiver et al.*'s [2001] software that is available from the University of Utrecht paleomagnetism laboratory website. In addition, an IRM acquired in a 325 mT field ($IRM_{325\ mT}$) was measured for 200 samples from the 200 to 350 m stratigraphic interval in order to activate only the low-coercivity components observed in IRM acquisition modeling. This field was also chosen because it is approximately the theoretical maximum coercivity for magnetite [*Butler*, 1992]. χ was also measured for these samples using a KLY-3S Agico susceptibility meter. The $\chi_{ARM}/IRM_{325\ mT}$ ratio over the 200–350 m interval, where χ_{ARM} is the ARM susceptibility (i.e., ARM normalized by DC bias field; χ_{ARM} = ARM/DC field) was calculated to quantify magnetic grain size variations. The IRM_{325mT}/χ ratio was used to determine the contribution of magnetic sulfides (pyrrhotite) to the low-coercivity components of magnetization [*Peters and Dekkers*, 2003].

[13] In order to calibrate the $IRM_{325\ mT}/\chi$ ratio for quantification of the amount of pyrrhotite in our Arguis Formation samples, we measured the ratio for samples we constructed with either 100% magnetite (equant and acicular) or 100% pyrrhotite, as the ferromagnetic mineral. We also constructed samples with mixtures of pyrrhotite and equant magnetite. The two mixtures measured are 50% pyrrhotite and 50% magnetite, by weight, and 70% pyrrhotite and 30% magnetite, by weight. Kaolinite clay was used as the nonmagnetic matrix (Twigg's County, Georgia, available from Ward's, National Science Establishment Inc., Rochester, NY). The proportion of ferromagnetic material was ≤1% by weight of the dry kaolinite used for our samples. The magnetic material and kaolinite were mixed as a dry powder and distilled water was added to make a slurry. The slurry was completely dried and the IRM in a 308 mT field (a saturation IRM) and low-field susceptibility were measured. The acicular magnetite used is 0.45 μm long with a length:width ratio of 6:1 (Pfizer MO-4232), the equant magnetite is 0.5 μm in diameter (Pfizer MO-7029). The pyrrhotite was naturally occurring and obtained from Alfa Aesar (Fe_7S_8, stock #42652, lot #H06P23; Ward Hill, MA 01835) as 1.5–4.75 mm pieces. It was ground to a powder using a mortar and pestle.

3.2. Cyclostratigraphy

[14] Our sampling strategy for rock magnetic cyclostratigraphy was designed to maintain a sampling interval of 4 kyr or less to ensure resolution of precession index variations in magnetic mineral concentration. An unoriented sample was collected every 20 cm from 0 to 100 m above the base of the Arguis, every 75 cm from the 100–500 m stratigraphic interval of the Arguis Formation, and every 1.5 m from 500 m to 800 m above the base of the section for a total of 1174 samples. The three adjustments in sample rate were made in response to field observations of increasing cycle thicknesses up section and the paleomagnetic results of *Hogan and Burbank* [1996]. Samples for magnetic cyclostratigraphic analysis were crushed and packed into 8 cm^3 plastic boxes for measurement and rock magnetic analysis. Each sample integrates approximately 2–3 centuries of time based on the formation's average sediment accumulation rate estimated from the

magnetostratigraphy. ARM was applied with an alternating field between 100 and 0 mT in the presence of a 97 μT DC field and mass normalized.

[15] The ARM data series was detrended in preparation for time series analysis by removing a 10% weighted mean from the data (*Cleveland* [1979], implemented in Kaleidagraph^{TM}). The ARM data series was then tied to absolute time using the magnetostratigraphy developed as a part of this study. To convert from stratigraphic position to time, a pointer series was generated using chron boundaries (Table 1). Chron boundary ages were taken from *Gradstein et al.* [2004]. These operations were conducted using Analyseries 2.0.4.2 [*Paillard et al.*, 1996].

[16] The ARM time series was resampled in equal intervals using a simple linear interpolation every 3.28 kyr. Spectral analysis employed the multitaper method (MTM) with 2π prolate multitapers using the SSA-MTM toolkit [*Ghil et al.*, 2002]. Robust estimation of background red noise with confidence limits at the 90%, 95%, and 99% level were determined following *Mann and Lees* [1996]. After Milankovitch frequencies were observed in the data a detailed chronostratigraphy was developed by tuning the filtered time series first to long eccentricity (405 kyr) and then to the full theoretical orbital eccentricity signal [*Laskar et al.*, 2004] in two iterations. Finally, coherency analysis was conducted using the Blackman-Tukey algorithm (Analyseries). The tuned ARM time series was compared to summer half-year insolation at the paleolatitude of the site in the Eocene.

3.3. Magnetostratigraphy

[17] A magnetostratigraphic study of the Arguis Formation was initially undertaken by *Hogan* [1993] and *Hogan and Burbank* [1996]. *Hogan and Burbank*'s [1996] (HB96) results show recovery of only eight reversal boundaries, out of fifteen reversal boundaries expected from the biostratigraphy. A detailed magnetostratigraphic study of the Arguis was conducted with the goal of refining HB96's magnetostratigraphy to provide higher stratigraphic resolution of the chron boundaries used to tie the ARM cyclostratigraphy to absolute time. This was accomplished by developing detailed sections across intervals where reversal boundaries had been reported previously and by narrowing the sampling interval. A total of four sections resulted. They were sampled at a mean spacing of ~3 m stratigraphically.

[18] Samples were obtained in the field with a portable, gasoline-powered sampling drill equipped with a 1 inch nonmagnetic diamond-tipped drill bit. Two to three individually oriented cores were collected at each horizon, which produced at least three standard paleomagnetic specimens (2.54 cm diameter, 2.1 cm long).

[19] Remanent magnetization during progressive demagnetization was measured with a three-axis 2G Enterprises superconducting magnetometer housed in a magnetically shield room (<200 nT) at the University of Michigan. Specimens were progressively stepwise demagnetized in an ASC Thermal Demagnetizer and for a smaller number of samples with a Sapphire AF (alternating field) demagnetizer. Characteristic remanent magnetizations (ChRMs) were determined for all specimens using principal component analysis (PCA [*Kirschvink*, 1980]). The latitude of the Virtual Geomagnetic Pole (VGP) was used to determine the polarity of the magnetostratigraphy.

4. Results

4.1. Magnetic Mineralogy

[20] Detailed modeling of IRM acquisition results for sample Fl9 (Figure 3a) are representative of all the IRM modeling results. Most IRM acquisition curves are best fit with two overlapping low-coercivity components that are consistently centered at ~30 mT and ~70 mT and one high-coercivity component that is weak and relatively poorly determined. The low-coercivity components contribute about 90% to the SIRM and become saturated by about 300 mT. The high-coercivity component in the IRM acquisition modeling averages about 675 mT, but ranges from as low as 286 mT to as high as 1120 mT. These coercivities are high enough that they will not be activated in the fields used for ARM acquisition (≤100 mT) and will not contribute to the ARM cyclostratigraphy.

[21] Thermal demagnetization of pARMs of 3 out of the 4 samples studied (Figure 4) indicates that both of the low-coercivity components (30 and 70 mT) are carried by a magnetic mineral with a remanence completely removed by 500°C to 550°C, most likely magnetite. The fourth sample studied by thermal demagnetization of ARM has a much stronger ARM (4 times) and clearly shows the presence of a magnetic mineral whose remanence is removed in the 300°–400° range for the 30–0 mT pARM, quite possibly a magnetic iron sulfide (Figure 4). In the

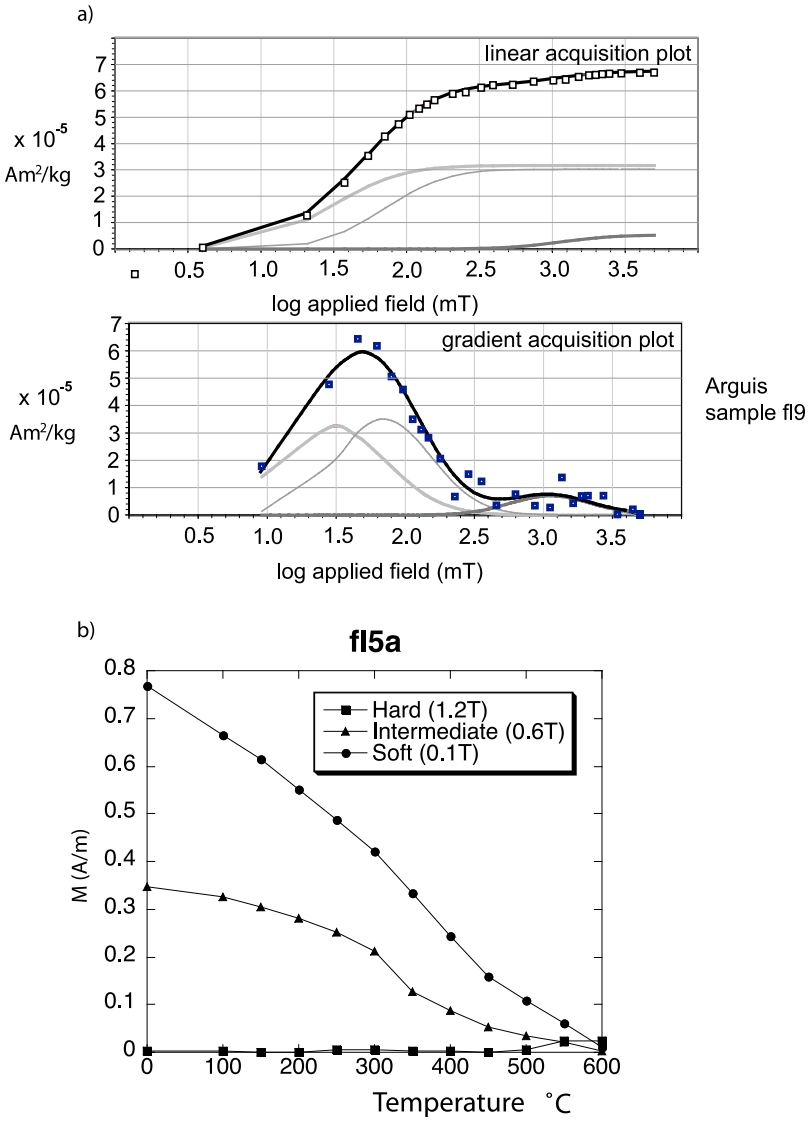

Figure 3. (a) Representative IRM acquisition modeling [*Kruiver et al.*, 2001] of a fine-grained marly sandstone from the Arguis formation. Shown are the linear IRM acquisition plot (LAP) and the gradient acquisition plot, which is the derivative of the LAP. (b) Representative thermal demagnetization of a three-component IRM [*Lowrie*, 1990] of a fine-grained marly sandstone from the Arguis.

Lowrie [1990] test (Figure 3b), all samples are completely demagnetized by 600°C. In many of the finer-grained lithologies, a drop in remanence is observed between 300° to 400°C for the intermediate coercivity component (0.1–0.6 T), additional evidence for the presence of iron sulfides. The softest IRM component (≤0.1T) behaves similarly to the pARM thermal demagnetization supporting the interpretation that a magnetic phase completely unblocked by a temperature near to 550°C, likely to be magnetite, carries the lowest-coercivity component. Very little magnetization was observed in the highest-coercivity component (0.6–1.2 T) used for the Lowrie test, consistent with the IRM acquisition modeling results.

[22] To confirm the presence of magnetic sulfides in the intermediate coercivity component (0.1–0.6 T), and check for the presence of maghemite, which also unblocks between 300°C and 400°C, two samples were remagnetized after thermal demagnetization in the same three orthogonal directions and fields. An increase in magnetization of approximately three orders of magnitude was observed for each component, suggesting the oxidation of a nonmagnetic mineral, most likely pyrite, to magnetite during the heating. The increase in remanence following

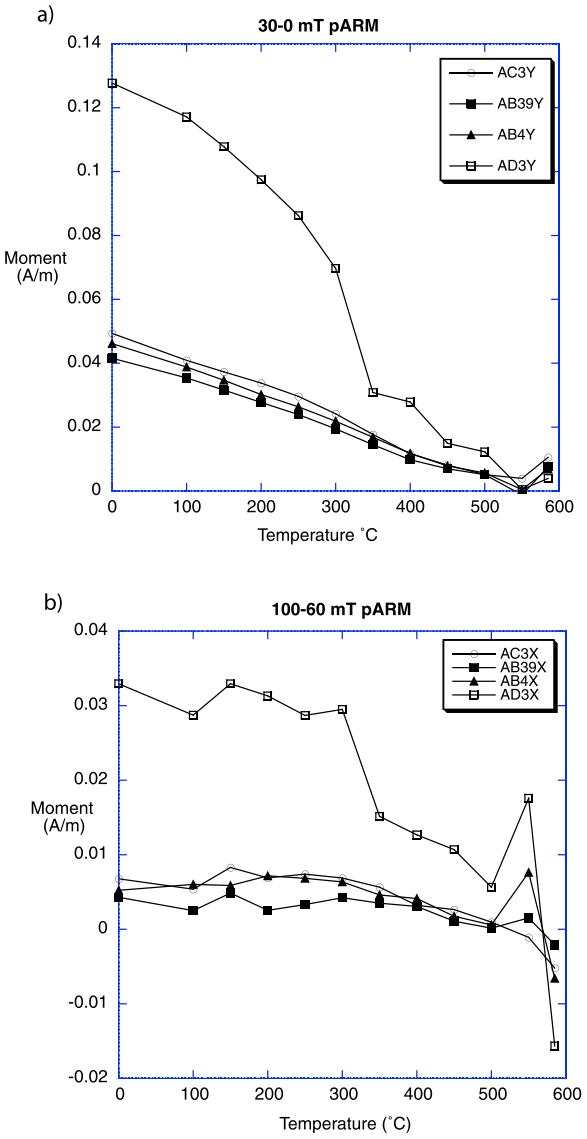

Figure 4. Thermal demagnetization of pARMs applied to four samples from throughout the complete Arguis Formation section: (a) pARM acquired between 30 and 0 mT and (b) pARM acquired between 100 and 60 mT. Note the strong evidence for magnetic sulfides in sample AD3 but not in the other samples. Samples AB4 and AB39 are from the 630–795 m interval, AC3 is from the 240–365 m interval, and AD3 is from the 160–220 m interval.

heating rules out the presence of maghemite in the Arguis samples because maghemite would invert to hematite after heating and have a much lower post-heating IRM.

[23] $IRM_{325\,mT}$ values range from 2.4×10^{-5} to 5.8×10^{-5} Am^2/kg and the ratio of IRM_{325mT}/χ ranges from 0.48 to 1.16 kA/m. When compared to experimental results for magnetic minerals summarized by *Peters and Dekkers* [2003], the IRM_{325mT}/χ ratio is consistent with the dominance of magnetite for the low-coercivity magnetic phases in the Arguis samples because the ratio is well below the ratio expected for magnetic sulfides (pyrrhotite or greigite). The dominance of magnetite is also supported by comparison to the IRM/χ ratios obtained from the artificial samples constructed with mixtures of pyrrhotite and magnetite (Table 2). The lowest IRM_{325mT}/χ ratio observed for our artificial samples was 6.23 kA/m for 100% equant magnetite, higher than the ratios for our natural Arguis samples.

[24] The χ_{ARM}/SIRM ratio over the 200–350 m interval was highest at the bottom of the interval with a value of 1.81×10^{-3} m/A. Its mean value decreased to about 1.3×10^{-3} m/A at 242 m and leveled out at about 1.22×10^{-3} m/A by 300 m.

4.2. Magnetostratigraphy

[25] The magnetostratigraphic study focused mainly on the gray siltstones and marls of the Arguis Formation and the very top of the underlying Guara Formation, because this is the same interval covered by HB96 and has the best exposure. Most of the samples were thermally demagnetized because alternating field demagnetization did not prove to be effective at isolating the characteristic magnetization (ChRM).

[26] Natural remanent magnetization (NRM) directions cluster around the present field direction revealing the presence of a persistent recent geomagnetic field overprint in the sediments. The average NRM intensity is moderate (0.181 mA/m) (Figure 5) similar to that observed by the previous paleomagnetic studies of the Arguis Formation [*Pueyo*, 2000; *Pueyo et al.*, 2002]. During thermal demagnetization a relatively low unblocking temperature overprint is usually present in most of the Arguis samples. In samples with normal polarity ChRMs the low unblocking temperature overprint is not well defined, but tends to be parallel to the

Table 2. IRM/χ Ratios for Pyrrhotite-Magnetite Mixtures in Artificial Sediments[a]

Magnetic Mineral(s)	IRM/χ (kA/m)
100% equant magnetite	6.23
100% acicular magnetite	12.18
50%–50% equant magnetite-pyrrhotite	17.07
70%–30% equant magnetite-pyrrhotite	23.48
100% pyrrhotite	67.80

[a]Magnetite-pyrrhotite mixtures are by weight. Kaolinite used for nonmagnetic matrix. Magnetic minerals are from 0.49% to 1.1% by dry sediment.

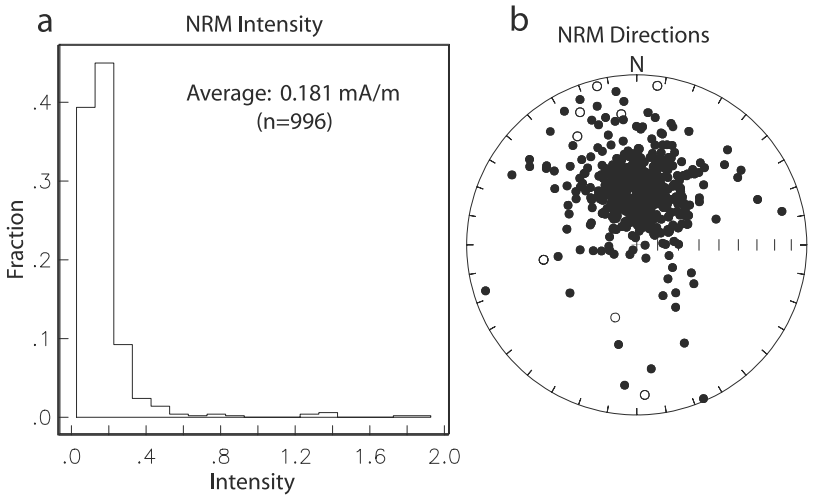

Figure 5. Natural remanent magnetization (NRM) data. (a) Histogram showing the variation of the initial intensity before demagnetization. (b) Distribution of NRM directions before demagnetization. Notice that directions cluster around the present-day field direction.

present-day geomagnetic field. Some samples display a relatively sharp decrease in intensity at 150°C to 200°C, followed by a progressive decay in intensity at temperatures up to 330°C to 380°C (Figure 6a). Very often, the magnetization becomes unstable at temperatures greater than 340°C precluding demagnetization at higher temperatures. An intensity decrease followed by instability in this temperature range suggests the presence of iron sulfides in the samples. This interpretation is confirmed by detailed rock magnetic analysis both in this study (see section 4.1) and by *Larrasoaña et al.* [2003].

[27] In order to determine the polarity of samples affected by unstable demagnetization behavior at intermediate temperatures close to 300°C, great circle analysis was used (Figure 6b) [*Kramow*, 1958; *Halls*, 1976]. The intersections of the remagnetization circles in stratigraphic coordinates are interpreted to be the high unblocking temperature magnetization of the samples. This interpretation is supported by comparing representative samples with high unblocking temperature reversed polarity magnetization components isolated by PCA to their corresponding remagnetization circles (Figure 6b). In these cases, the magnetization vector moves along the remagnetization circle toward a south and up direction. The validity of using remagnetization circles to isolate the primary magnetization of the Eocene marls and siltstones in the region was already demonstrated by *Pueyo et al.* [2002] and *Larrasoaña et al.* [2003] who successfully retrieved primary magnetization directions. The one site studied from the Guara limestone (sample GU1-02A in Figure 6b), shows a more resistant overprint that is not removed at 380°C. Above this temperature, the magnetization direction becomes erratic and great circle analysis is the only method that can determine the high-temperature magnetization component.

[28] Rock magnetic measurements, both *Lowrie* [1990] tests and IRM_{325mT}/χ ratios (section 4.1), indicate that magnetite is the carrier of both the ARM cyclostratigraphy in the Arguis Formation; however, the presence of iron sulfides that plagued the thermal demagnetization results would suggest that in some parts of the section the iron sulfides, rather than magnetite, carry the magnetostratigraphy since their decomposition during heating obscures the resolution of the remanence carried by the magnetite.

[29] ChRMs were successfully isolated in most sites, allowing the determination of a magnetostratigraphy for the Arguis Formation (Figure 7). The Arguis magnetostratigraphy reveals at least eleven magnetozones, labeled R1 through R6 and N1 through N5. The midpoint stratigraphically between two successive sites of opposite polarity was chosen as the position of the chron boundary. A minimum of two consecutive horizons was used to establish the presence of a polarity chron in establishing the magnetostratigraphy.

4.3. Cyclostratigraphy

[30] ARM values range from 1.1×10^{-6} to 1.0×10^{-5} Am^2/kg with obvious variability in the 5–10 m wavelength scale (Figure 8a). MTM spectral analysis of the detrended ARM data series (Figure 8b),

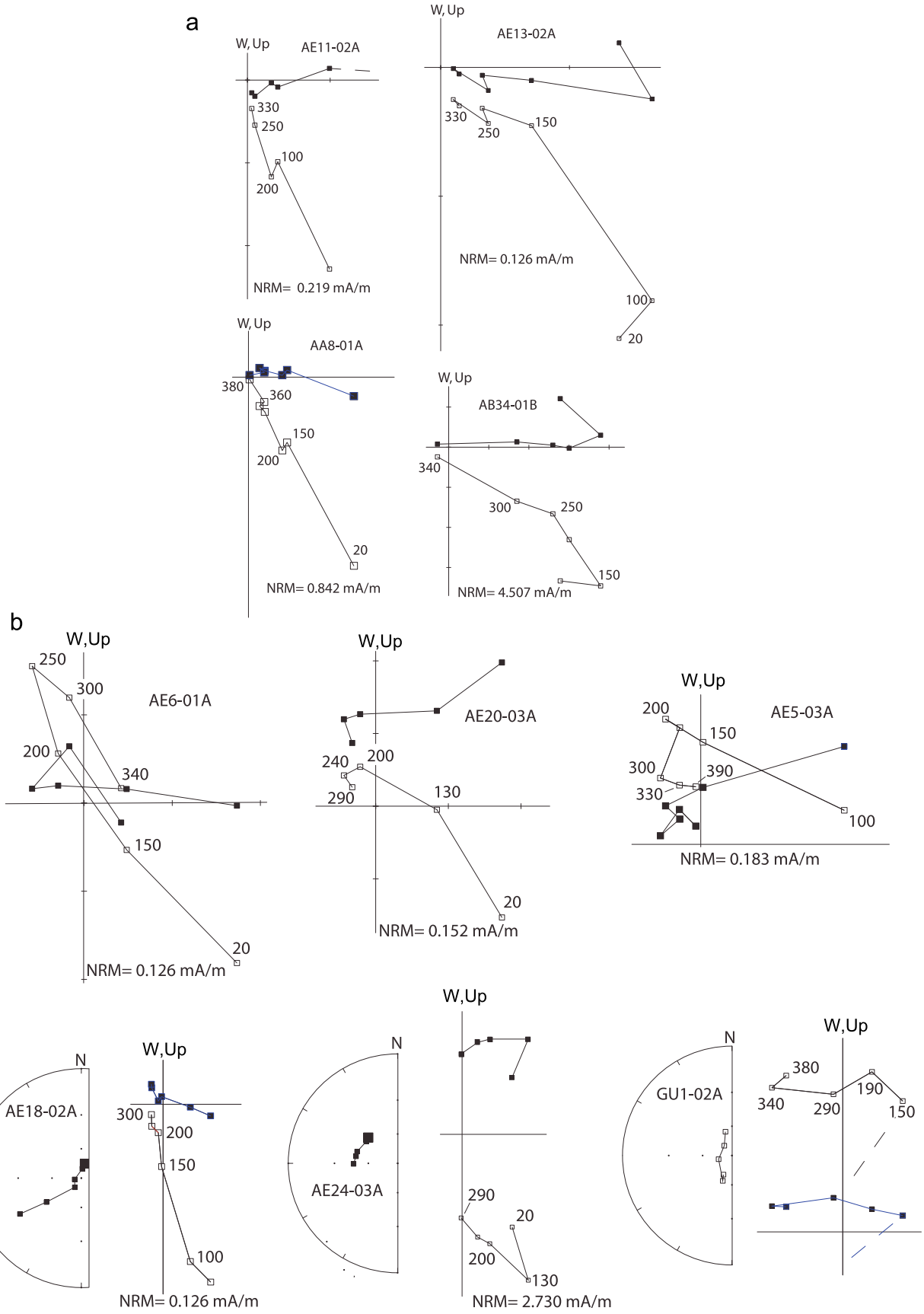
a
W, Up
AE11-02A
330
250
100
200
NRM= 0.219 mA/m
W, Up
AE13-02A
330
250
150
NRM= 0.126 mA/m
100
20
W, Up
AA8-01A
380
360
150
200
20
NRM= 0.842 mA/m
W, Up
AB34-01B
340
300
250
150
NRM= 4.507 mA/m
b
W,Up
250
300
AE6-01A
200
340
150
20
NRM= 0.126 mA/m
W,Up
AE20-03A
240
200
290
130
20
NRM= 0.152 mA/m
W,Up
200
150
AE5-03A
300
390
330
100
NRM= 0.183 mA/m
N
AE18-02A
W,Up
300
200
150
100
NRM= 0.126 mA/m
N
AE24-03A
W,Up
290
20
200
130
NRM= 2.730 mA/m
N
GU1-02A
W,Up
380
190
340
290
150

Figure 6

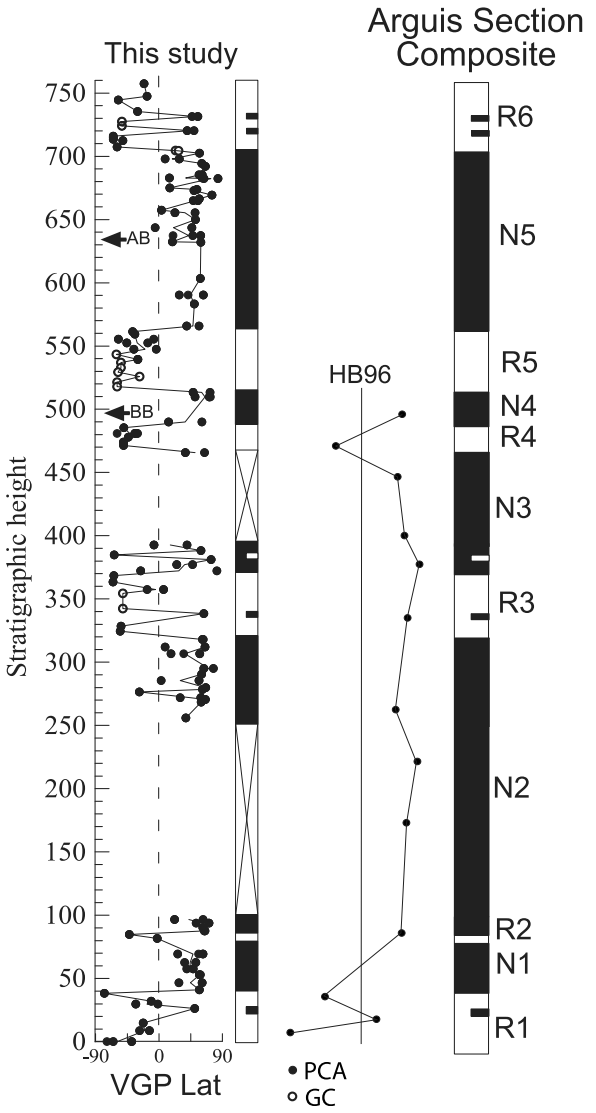

Figure 7. Virtual geomagnetic pole (VGP) latitudes and composite magnetostratigraphy for the Arguis Formation based on this study and HB96. Sites that have an opposite polarity to those sites directly above and below stratigraphically have been represented with a half-length line on the composite magnetostratigraphy. HB96 represents the approximate location of the paleomagnetic results by *Hogan and Burbank* [1996]. AB, Arguis Bed; BB, Bryozoan Bed (see Figure 2). Solid circles indicate sites determined by principal component analysis (PCA), and open circles indicate sites determined by great circle analysis (GC).

converted to periodicity with the average accumulation rate indicated by the magnetostratigraphy, shows significant power in the precession index band, as well as at short eccentricity (125 kyr and 80 kyr, near to 95 kyr), and long eccentricity (405 kyr).

[31] One of the primary goals of this work is to develop a high-resolution chronostratigraphy for the Arguis Formation. The untuned ARM time series already shows the presence of Milankovitch periodicities in its spectral analysis (Figure 8). In order to further reduce the effects of variability in sedimentation rate during deposition of the Arguis Formation on the time-frequency analysis and to obtain the best absolute ages and age resolution for the Arguis section, the ARM data were tuned to the orbital eccentricity signal predicted over this geological interval [*Laskar et al.*, 2004].

[32] First, a low-pass Taner filter (f_{cut} = 0.004 cycles/kyr, see Figure 10a) [*Taner*, 2000] was applied to isolate 405 kyr cycles in the data. The 405 kyr minima in the filtered data were used to scale the time series to 405 kyr intervals (Figure 9a). The spectrum redistributes power into a narrow band at 405 kyr, and into a somewhat broader (but lower power) band centered at 129 kyr; significant power occurs also in the precession index band (Figure 10a). This 405 kyr tuned ARM time series was then scaled to the orbital eccentricity model of *Laskar et al.* [2004] by matching the minima of visually identified 100 kyr cycles to the minima in the *Laskar et al.* [2004] theoretical eccentricity series (Figure 9a; spectrum in Figure 10b). This eccentricity-scaled ARM time series was then low-pass Gauss filtered (f_{cut} = 0.025 cycles/kyr; see Figure 10b) to more clearly isolate the eccentricity band. These filtered data were tuned again to the eccentricity, this time using both minima and maxima (Figure 9c); the spectrum reflects improved spectral peaks, as expected, at 400 kyr, 122 kyr and 94 kyr (Figure 10c). The spectra generated from all of the ARM time series show strong peaks at 400 kyr (long eccentricity) 128 and 95 kyr (short eccentricity) and 23, 22, and 19 kyr (precession), that all rise above the 99% confidence limit of robust red noise.

Figure 6. Results of progressive thermal demagnetization data for Arguis Formation samples and one sample from the Guara Formation limestone displayed by vector endpoint diagrams [*Zijderveld*, 1967] of representative samples. Each data point represents endpoint vectors for individual demagnetization steps projected onto the horizontal (solid symbols) and vertical (open symbols) plane. Numbers adjacent to magnetization directions indicate the demagnetization temperatures in degrees Celsius. (a) Normal polarity samples showing a large decrease in intensity between 100°C and 150°C and final temperatures > 400°C. (b) Reversed polarity samples from vector endpoint diagrams and remagnetization circle analysis.

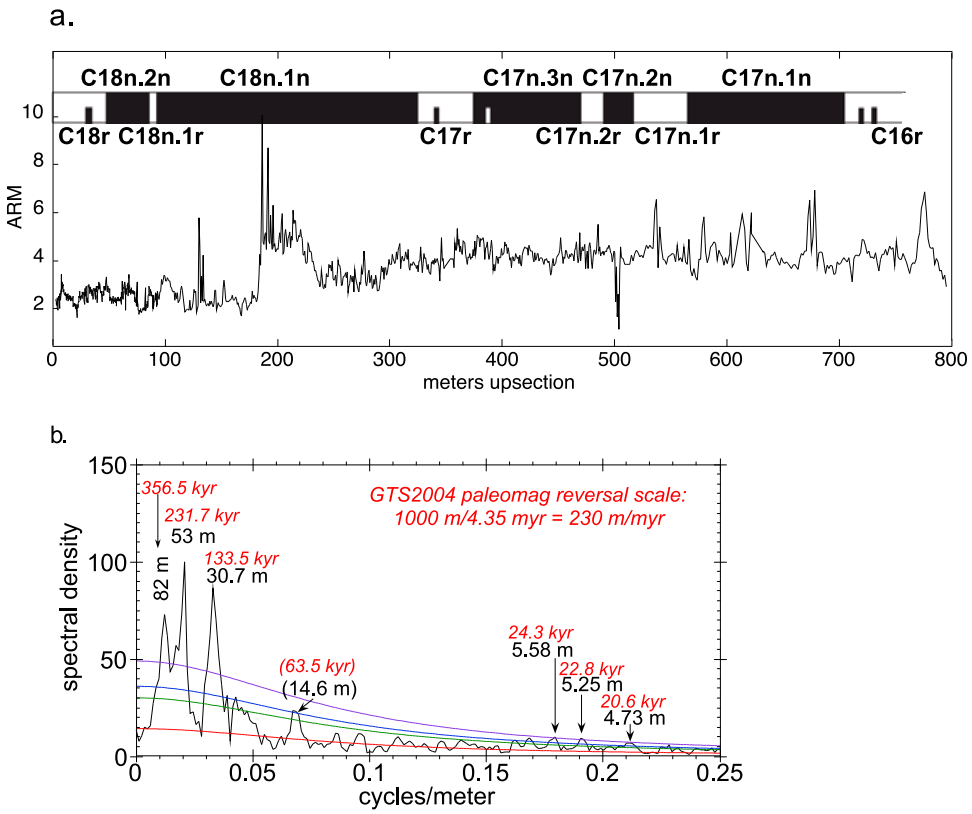

Figure 8. (a) Mass normalized ARM data series for 800 m of the Arguis Formation. The interpreted chrons are shown at the top; chron boundary ages are given in Table 1. (b) MTM spectral analysis of the ARM data series after removal of a 10% weighted mean. The red curve indicates the robust red noise [*Mann and Lees*, 1996]; the green, blue, and purple curves indicate 90%, 95%, and 99% confidence limits. Significant peaks are identified in terms of thickness; the average sedimentation rate according to the geomagnetic polarity time scale GPTS2004 calibrates these peaks close to expected Milankovitch periodicities (also shown).

[33] Coherency analysis shows that the eccentricity-tuned ARM time series is coherent not only in the tuned eccentricity band, but also in the untuned precession index band, with nonzero phasing (Figure 11a). The precession index is 2 to 2.5 radians out of phase with summer half-year insolation at 35°N, the paleolatitude of the site in the Eocene based on *Besse and Courtillot*'s [2002] synthetic apparent polar wander path for Europe. In sum, the coherency analysis between summer half-year insolation and monthly insolation at 35°N shows that October and November insolation is 2 to 2.5 radians out of phase with summer half-year insolation (Figure 11b). By inference, this means that the eccentricity-tuned ARM time series is in phase with October–November insolation at 35°N during the Eocene. This information is used to understand the climate encoding by ARM in the Arguis Formation (discussed further below).

5. Discussion

5.1. Magnetic Mineralogy

[34] All the rock magnetic measurements support the interpretation that magnetite is the dominant magnetic phase that carries the ARM cyclostratigraphy. The 200 IRM_{325mT}/χ values that range

Figure 9. Time scale development of the Arguis series. (a) The Arguis time series according to GPTS2004 ages (Table 1). (b) The 405 kyr tuned Arguis time series, with 405 kyr tie points indicated by vertical gray lines. The low-pass Taner filter (passband in Figure 10a) isolates 405 kyr cyclicity in the Arguis series. (c) La2004 eccentricity-tuned time series, first iteration. La2004 eccentricity series is shown with gray vertical tie lines between Arguis ARM minima and eccentricity minima. (d) La2004 eccentricity tuning, second iteration. Minima and maxima of the low-pass filtered ARM series (filter passband in Figure 10c) are tied to minima and maxima of the eccentricity series, shown with gray vertical tie lines. Small "e" designates ~100 kyr cycles through the series. (e) La2004 eccentricity-tuned accumulation rates defined at ~50 kyr intervals along the Arguis series.

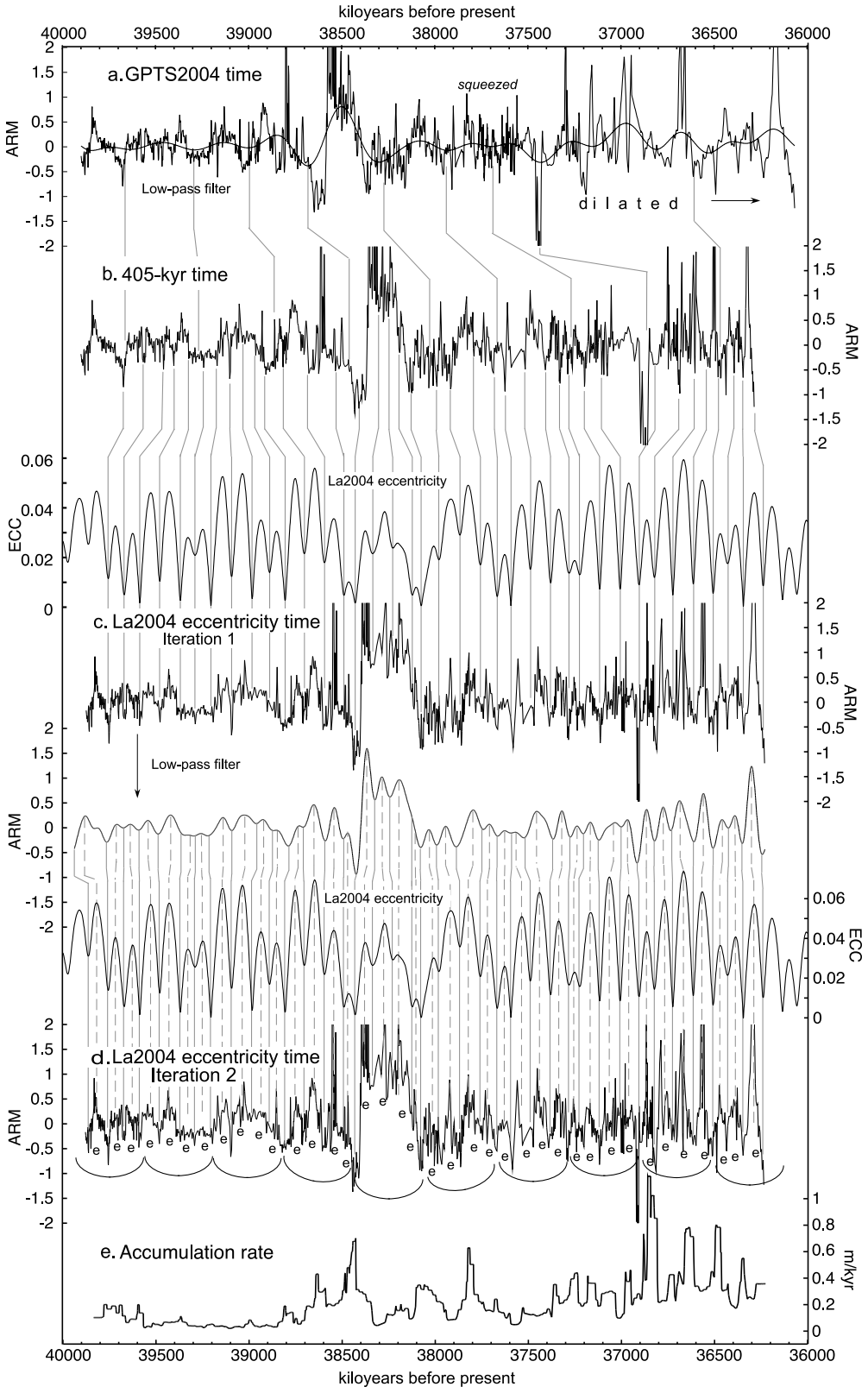
kiloyears before present
40000
39500
39000
38500
38000
37500
37000
36500
36000
a. GPTS2004 time
squeezed
Low-pass filter
d i l a t e d
ARM
b. 405-kyr time
La2004 eccentricity
ECC
c. La2004 eccentricity time
Iteration 1
Low-pass filter
d. La2004 eccentricity time
Iteration 2
e. Accumulation rate
m/kyr

Figure 9

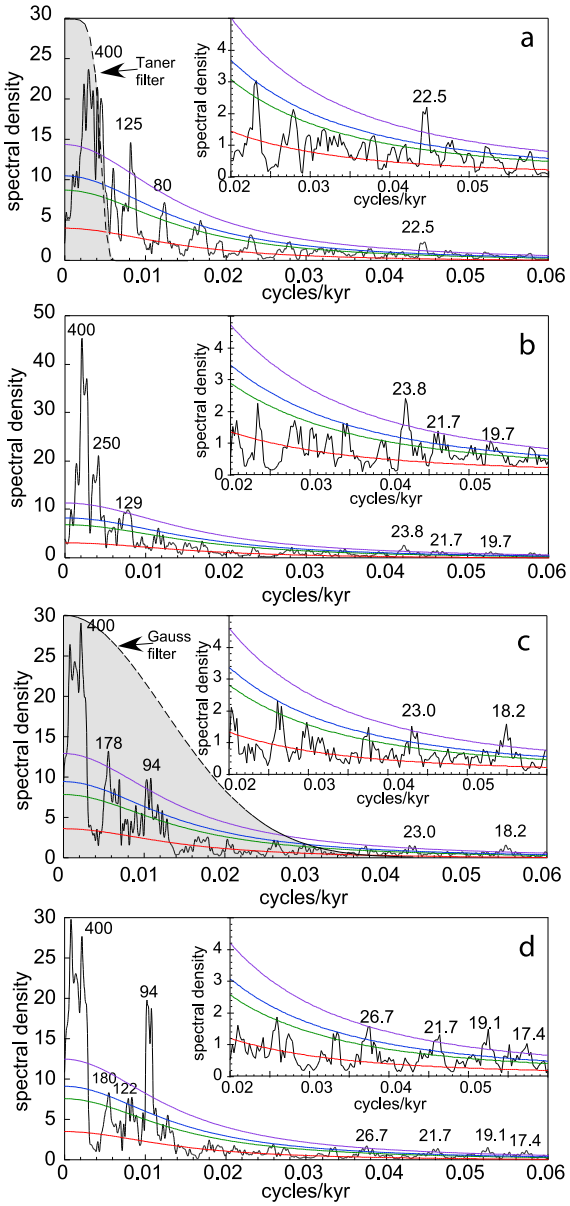

Figure 10. Spectral analysis of the eccentricity-tuned Arguis series, using orders 0–2 2π prolate multitapers and robust red noise (log fit) modeling (SSA-MTM toolkit). Red curves are robust red noise fits; green, blue, and purple curves indicate 90%, 95%, and 99% confidence limits. All labeled spectral peaks are in kiloyears. The insets zoom in on the frequency range from 0.02 to 0.06 cycles/kyr. (a) GPTS2004-tuned spectrum. The Taner low-pass filter (fcut = 0.004 cycles/kyr) has a steep stopband to isolate 405 kyr cyclicity in the series. (b) The 405 kyr tuned spectrum. (c) La2004 eccentricity-tuned (first iteration) spectrum. The Gauss low-pass filter (fcut = 0.015 cycles/kyr) is used to filter out high frequencies and to isolate eccentricity band signal with a gradual stopband to account for potentially large variations in accumulation rate (and misaligned frequency components) remaining in the time scale. (d) La2004 eccentricity-tuned (second iteration) spectrum.

from 0.48 to 1.16 kA/m are quite low and consistent with magnetite for the low-coercivity phases (<325 mT) [*Peters and Dekkers*, 2003] (Table 2). The thermal demagnetization of the 0.1 T IRM and the 100–60 mT and 30–0 mT pARMs also support the presence of magnetite for the low-coercivity phases in the rock (Figures 3b and 4) and the lack of dominant contributions by magnetic sulfides. The IRM_{325mT}/χ ratio must be used with caution, since susceptibility measures not only the ferromagnetic minerals, but also the paramagnetic and diamagnetic minerals in a sample. The Arguis Formation consists mainly of quartz and calcite nonferromagnetic matrix grains, both diamagnetic minerals. If these minerals were to contribute significantly to the susceptibility, the susceptibility values would be low and the IRM_{325mT}/χ ratio correspondingly higher than that due to a pure ferromagnetic measurement. Despite the presence of diamagnetic minerals, the IRM_{325mT}/χ ratio is low, so the diamagnetic minerals could not appreciably mask the contribution of sulfides to the low-coercivity remanence.

[35] Thermal demagnetization of a three-component IRM indicates the presence of two different magnetic phases in the intermediate coercivity (0.1–0.6 T) range (Figure 3b). Based on unblocking temperatures of ~300°C and ~ 550°C these phases are magnetite and a magnetic sulfide, either pyrrhotite or greigite. Based on the intermediate coercivity of this phase, pyrrhotite is the preferred interpretation [*O'Reilly*, 1984]. The thermal demagnetization of pARMs supports the thermal demagnetization of the three component IRM, but does show for one sample studied the presence of a magnetic sulfide at low coercivities (30–0 mT); however, the IRM_{325mT}/χ ratios for the 200 samples from 200 m to 350 m in the section indicates that the sulfides typically have higher coercivities, >325 mT, and should not be an important contributor to the ARM.

[36] IRM acquisition modeling (Figure 3a) indicates the presence of a high coercivity magnetic phase in many of the samples. The coercivity of this phase is not well constrained and varies from as low as 286 mT to as high as 1120 mT for the samples studied. In some cases, for coercivities less than 600 mT, this phase is probably pyrrhotite, but for higher coercivities this phase may be goethite. The evidence supporting this interpretation is that the Lowrie test shows the loss of all remanence by 600°C, which is well below the Curie temperature for hematite (680°C), and thermal demagnetization for the magnetostratigraphic study indicates occasional relatively sharp decreases in intensity below 200°C

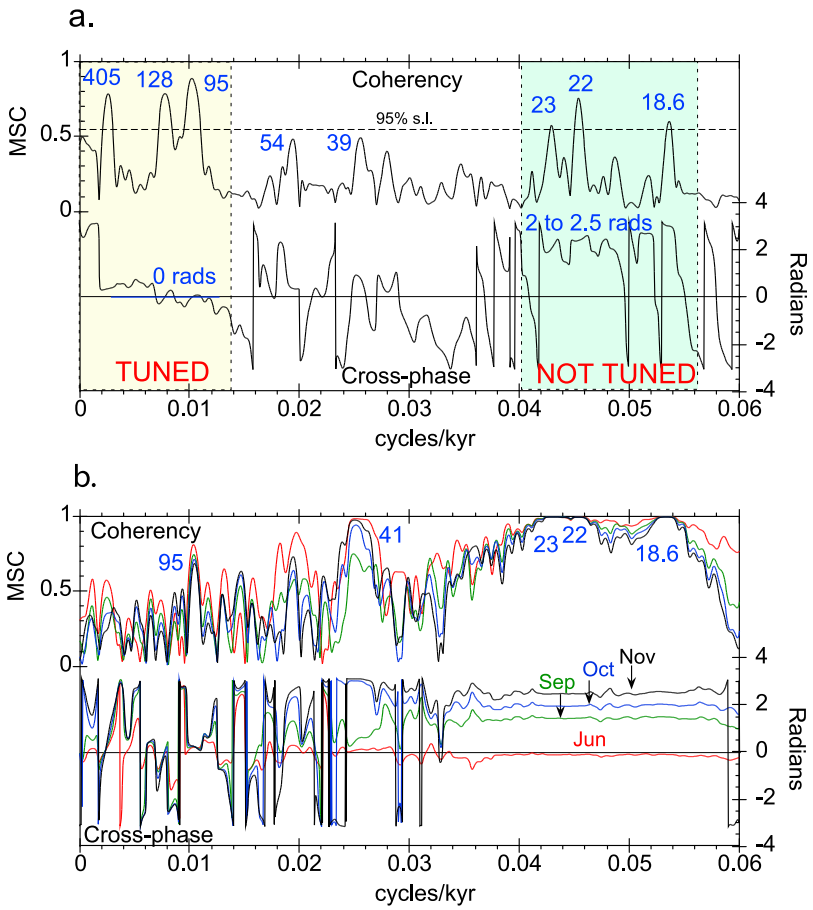

Figure 11. Coherency and cross-phase spectral analysis of insolation versus eccentricity-tuned ARM time series, using the Blackman-Tukey algorithm with 30% lags and Bartlett windowing (in Analyseries). (a) Summer half-year insolation at 35°N (calculated in Analyseries) versus eccentricity-tuned ARM time series, from 36,230 ka to 39,875 ka. Magnitude-squared coherency (MSC) with labeled peaks in kiloyears is shown at the top; the cross phase (in radians) is shown at the bottom. Note that the precession index band has not been tuned, yet it shows elevated coherency and flat cross phase through the band. (b) Summer half-year insolation at 35°N (from Analyseries) versus monthly insolation at 35°N from 36,230 ka to 39,875 ka. Coherency and cross-phase spectra are shown for the months of June, September, October, and November. Note the advance in cross phase in the precession index band for these months.

(Figure 6a). The high coercivity of this phase ensures that it has not contributed to the ARM cyclostratigraphy.

[37] The IRM acquisition modeling indicates that there are two low-coercivity phases (~30 mT and ~70 mT) with overlapping coercivity spectra. This is surprisingly similar to the biogenic soft (BS ~40 mT) and biogenic hard (BH ~ 70 mT) components observed by *Egli* [2003] for recent, anoxic lake sediments and attributed to magnetosomes generated by magnetotactic bacteria. However, the χ_{ARM}/SIRM ratios observed for the 200 samples from 200 m to 350 m in the section are not consistent with a major contribution to the remanence from magnetosomes. Although at 200 m χ_{ARM}/SIRM ratios could be due to magnetosomes (χ_{ARM}/SIRM = 1.81×10^{-3} m/A; ARM/SIRM = 0.14) the ratio quickly drops up section to values (χ_{ARM}/SIRM = 1.3×10^{-3} m/A; ARM/SIRM~0.1) more indicative of detrital, inorganic magnetite [*Moskowitz et al.*, 1993].

[38] In a study of Cretaceous carbonates from northeastern Mexico, *Latta et al.* [2006] considered eolian dust to be the source of the magnetite that carried the cyclostratigraphy. Unfortunately, the range in χ_{ARM}/SIRM ratios from 1.2 to 1.8×10^{-3} m/A for the Arguis is not strongly diagnostic for distinguishing between a fluvial and eolian source for the Arguis Formation magnetite. χ_{ARM}/SIRM ratios between about 0.25 and 1.25×10^{-3} m/A appear to be diagnostic of the magnetite in eolian dust collected from the northern Atlantic Ocean and the island of Barbados [*Oldfield et al.*, 1985], and

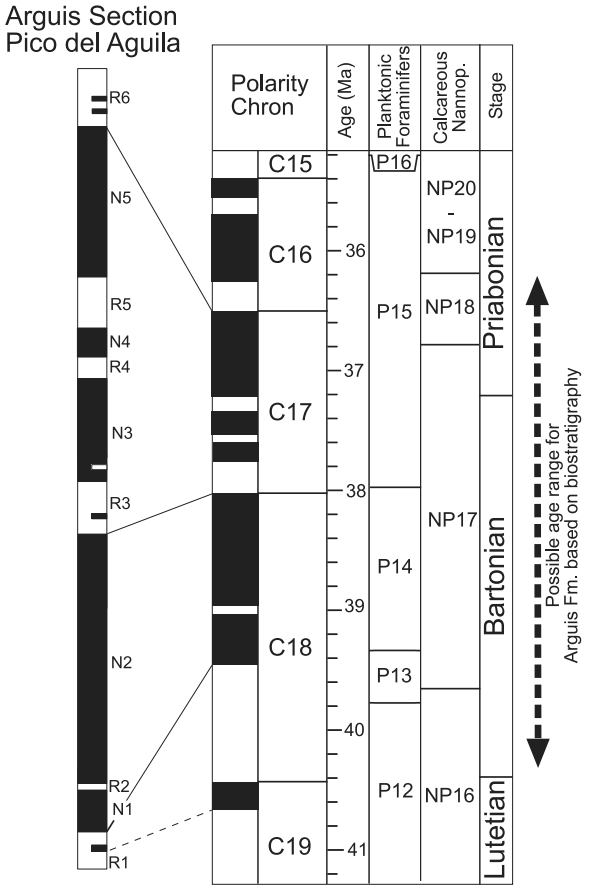

Figure 12. Correlation of the Arguis Formation magnetostratigraphy to the GPTS. Possible age range is constrained by the biostratigraphic record [*Canudo et al.*, 1988; *Canudo*, 1990; *Serra-Kiel et al.*, 1998] which is shown by the vertical line on the right.

from Indian Ocean deep-sea sediments with titanomagnetites derived from eolian dust [*Hounslow and Maher*, 1999]. Therefore, the Arguis χ_{ARM}/SIRM ratios are somewhat higher, with some overlap, than the ratios collected from unequivocally eolian sources. The higher χ_{ARM}/SIRM ratios of the Arguis Formation are most consistent with the ratios of fluvially derived sediments from off the southwestern coast of India ($1.0–2.0 \times 10^{-3}$ m/A [*Kumar et al.*, 2005]). In contrast, Yellow River sediments yield lower ratios similar to eolian sources ($0.1–0.9 \times 10^{-3}$ m/A [*Zhang et al.*, 2008]). One point that should be kept in mind is that the Arguis Formation sediments are interpreted to be deltaic in origin so a fluvial source for the magnetite is also consistent with the sediments' environment of deposition. Furthermore, *Sloan and Huber* [2001] show substantial continental runoff variability at precessional frequencies in the Eocene along the western European margin.

[39] A rock magnetic study performed on the Pamplona Marls, a more distal facies correlative to the Arguis Formation, also shows magnetite and pyrrhotite [*Larrasoaña et al.*, 2003]. In the Pamplona Marls, *Larrasoaña et al.* [2003] suggest that both magnetite and pyrrhotite carry a primary remanence based on a fold test. Larrasoaña et al. rule out greigite as the magnetic iron sulfide in the Pamplona-Arguis Marls based primarily on low-temperature magnetic behavior. This is consistent with our interpretation of the magnetic mineralogy in the type Arguis Formation in the Arguis syncline.

5.2. Correlation of the Magnetostratigraphy to the GPTS

[40] The magnetostratigraphic sampling was designed so that the results would complement those of *Hogan and Burbank* [1996] (HB96) and *Pueyo et al.* [2002]. The resulting magnetostratigraphic composite section (Figure 7) is based on this study's paleomagnetic results combined with HB96 for the lower half of the Arguis section, where HB96's results were unambiguously confirmed by field identification of their sites and subsequent laboratory measurements (Figure 7). The resulting composite magnetic reversal stratigraphy shows a total of six reversed polarity and five normal polarity chrons in the Arguis stratigraphic section. The composite magnetic reversal stratigraphy begins in the uppermost part of the Guara limestone, the location of this study's lowest paleomagnetic site.

[41] Due to the occurrence of numerous calcareous nanofossils and planktonic foraminifera in the Arguis, several biozones have been defined. These biozones allow the composite reversal magnetic stratigraphy developed here to be tied to the Geomagnetic Polarity Time Scale [*Gradstein et al.*, 2004]. The Arguis biostratigraphic record spans from the top of biozone NP16 to biozone NP18, or across the Bartonian/Priabonian boundary [*Canudo et al.*, 1988; *Canudo*, 1990; *Sztrákos and Castelltort*, 2001] (Figure 12). HB96 reported only four reversals which they interpreted as Chrons C18r to C17n based on earlier biostratigraphic constraints. This study's site spacing of 3 m, instead of HB96's 60 m, allowed determination of a more detailed reversal stratigraphy, in addition to the use of detailed progressive thermal demagnetization, instead of the blanket demagnetization used in the HB96 study.

[42] The composite reversal stratigraphy is correlated to the GPTS following these interpretations (Figure 12): Chron R1 is interpreted as being C18r. Normal chrons N1 and N2 would therefore corre-

spond to C18n.2 and C18n.1n, respectively. Reversed chron R3 would be C17r, with a lower boundary corresponding to the limit between planktonic foraminifer zones P14 and P15. The entire Chron17 appears to be present and its upper boundary with Chron C16r is found at a stratigraphic position of 705 m, in the uppermost part of the Arguis Formation.

[43] The biostratigraphic rationale for this correlation to the GPTS is as follows: The biostratigraphy, based on planktonic foraminifera, calcareous nanoplankton, and benthic foraminifera, indicates correlation to biozone NP17, which spans Chrons C18r to C17n.1n in the GPTS. In the underlying Guara limestone there are benthic foraminifera indicative of a Lutetian age (Chrons C18 and C19). The upper part of the Guara Formation contains nummulites *N. deshayesi* and *N.* aff. *bullatus*, which are the Lutetian precursor species of the Bartonian *N. perforatus* that appears in the lowermost part of the Arguis Formation [*Schaub*, 1981; *Canudo et al.*, 1988]. *N. striatus* is present in both the Arguis Formation and overlying Belsue-Atares Formation and correlates directly to biozones P15, NP17 and NP18 [*Canudo et al.*, 1988; *Serra-Kiel et al.*, 2003]. The upper part of the Arguis Formation has nanoplankton indicative of biozone NP17 [*Canudo et al.*, 1988]. These microfossiliferous and macrofossiliferous assemblages constrain the age of the Arguis and overlying Belsue-Atares Formations to be between Chrons C18 and C16. The bottom 80 m of the Arguis Formation has frequent glauconitic sandstones and is interpreted to be a "flooding surface" by *Castelltort et al.* [2003] Glauconitic sediments are typically associated with slow sedimentation rates and therefore condensed stratigraphic sections that are related to maximum flooding surfaces. Consequently, geomagnetic polarity chrons are expected to be stratigraphically thinner in this part of the section and explains why R1, correlated to C18r, is so thin stratigraphically.

[44] However, the correlation of R1 to the GPTS is less certain than our correlation for the rest of the section. The biostratigraphy suggests that the R1/N1 chron boundary corresponds to the C18r/C18n.2n boundary in the GPTS. Approximately 30 m from the top of the Guara limestone, directly underlying the Arguis Formation, the rocks are reversed polarity and are interpreted to be Chron C19 [*Rodriguez-Pintó et al.*, 2006]. Lutetian species such as *N. deshayesi* and *N. bullatus* [*Canudo et al.*, 1988] supports this interpretation. Furthermore, the results by *Rodriguez-Pintó et al.* [2006] also identify Chrons C20r and C21n lower in the Guara. Consequently, our preferred interpretation is that the short normal polarity interval at 25 m, based on only one horizon, corresponds to a very short event not recognized in the GPTS, rather than C19n. The short normal polarity interval could also be due to our inability to successfully remove the normal overprinting prevalent in the Arguis section. An unconformity at the Guara/Arguis contact [*Millan et al.*, 1994] could be the reason for the missing C19n chron, unless subsequent work finds it in the topmost 30 m of the Guara Formation.

5.3. ARM Cyclostratigraphy

[45] A robust cyclostratigraphy, with spectral peaks at the expected Milankovitch frequencies, has been developed in the Arguis Formation marls based on variations in ARM intensity. In the Arguis Formation, rock magnetic data indicate that the ARM measures concentration variations of low coercivity, most likely inorganic, detrital fluvial magnetite (see section 5.1). Therefore, the cyclostratigraphy is based on concentration variations of primary, depositional magnetite indicating that the fluvial supply of magnetite to the sedimentary basin appears to be driven by variations in global climate processes.

[46] The magnetite in the Arguis Formation is primary and probably originated from a detrital source for two reasons. First, evidence from the χ_{ARM}/SIRM ratios from the bottom half of the section and from low-temperature and hysteresis measurements on the correlative Pamplona Marls argues against magnetosomes as a significant magnetic carrier. Second, shallow (~3 km) burial conditions (*Hogan and Burbank*, 1996) and geothermal gradients (~15°C/km) [*Holl and Anastasio*, 1995] were not 1conducive to diagenetic magnetite formation [*Larrasoaña et al.*, 2003].

[47] Intermediate coercivity pyrrhotite is also present in the Arguis Formation marls, although it probably contributes little to the cyclostratigraphy. The petrographic observation of paramagnetic pyrite implies the presence of other iron sulfides throughout the Arguis Formation as both are formed through the same diagenetic process. Iron sulfides form in many marine sediments under anoxic, sulfate-reducing conditions through the process of pyritization [*Berner*, 1972, 1984], so the presence of magnetic sulfides is not unexpected. Remains of organic material (fossils, grazing and burrowing trails), prevalent iron oxides, and ubiquitous sulfate in marine waters from Triassic gypsum of the Keuper facies [*Anastasio*, 1992] make the Arguis

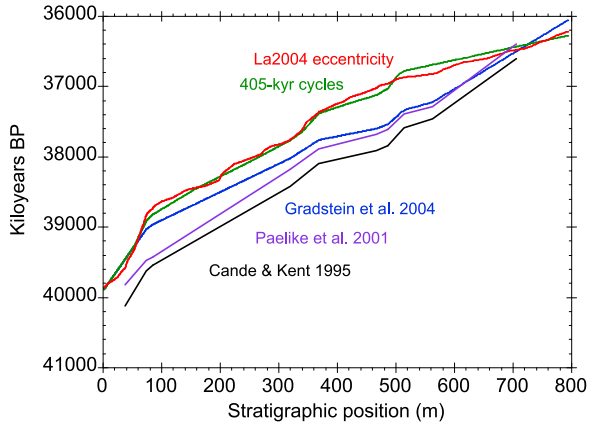

Figure 13. Comparison of chronologies applicable to the Arguis formation. The bottom three curves are magnetostratigraphic time scales, while the top two are from the tuning results from this study.

Formation conducive to iron sulfide precipitation. However, the extensive production of magnetic sulfides was probably prevented by the relatively rapid sedimentation rates (~0.2 m/kyr), causing reactive magnetite to pass through the zone of sulfate-rich pore fluid quickly and stopping the pyritization process from reacting to completion.

[48] Eccentricity tuning is important to the successful development of the Arguis Formation ARM cyclostratigraphy. Tuning the filtered ARM data series to orbital eccentricity modeled for the Eocene has allowed correction for variable sediment accumulation rates between chron boundaries. By tuning the ARM data series, relative time can be resolved throughout the Arguis Formation with a precision of 50 kyr resulting in a chronology that is synchronous with the *Gradstein et al.* [2004] time scale for the bottom 70 m of the Arguis (Figure 13). However, our chronology is younger than Gradstein et al.'s by about 200 kyr from 75 to 370 m in the section, then by 400 kyr from 370 to 500 m in the section. The ARM chronostratigraphic chronology comes back in congruence with Gradstein et al.'s chronology at about 700 m near the top of the section. The Gradstein et al. chronology is consistently younger than both *Pälike et al.* [2001] and *Cande and Kent*'s [1995] chronologies for this time interval in the Eocene, and our chronology deviates by almost 1000 kyr from them over extended portions of this interval.

[49] The 200–400 kyr offsets between our interpreted Arguis astrochronology and *Gradstein et al.*'s [2004] reference chronology occur at chron boundaries identified by the magnetostratigraphy. The first offset occurs at the C18n.2n-C18n.1r chron boundary, the second offset occurs at the C17r-C17n.3n chron boundary, and a return to synchrony occurs at the C17n.1n-C16r chron boundary (Figures 8 and 13). Between the two older offsets the ARM chronostratigraphy remains essentially parallel to the Gradstein *et al.* chronology.

[50] One explanation for these offsets is that the chron boundaries in this part of the Eocene are not known accurately. For example, *Cande and Kent*'s [1992, 1995] chron boundary ages are radiometrically calibrated at only 9 points; none occur in the time period covered by the Arguis Formation. Those closest to the Arguis Formation are situated at C13r(0.14) (33.7 ± 0.4 Ma) and C21n(0.33) (46.8 ± 0.5 Ma). *Cande and Kent* [1992] also indicate magnetic anomaly thickness errors for chrons 18n, 17, and 16 of 6.9%–6.1%; these together with ~1% tie point age errors indicate Eocene chron boundary age (2σ) uncertainties on the order of 500 kyr [*Agrinier et al.*, 1999]. *Gradstein et al.*'s [2004] Eocene chron ages are based on *Cande and Kent* [1995] with adjustments from *Wei* [1995] and *Berggren et al.* [1995] and in the argon dating of the Fish Canyon Tuff– Sanidine (FCT-SAN) monitor. *Pälike et al.*'s [2001] chronology is tuned astronomically, with Milankovitch cycles observed by XRF counts of iron and calcium in deep-sea sediments. *Pälike et al.* [2001] used their tuning to refine the Cande and Kent time scale; Gradstein et al.'s chronology was the starting point for this study.

[51] An alternate explanation for the offset between our interpreted ARM cyclostratigraphy and *Gradstein et al.*'s [2004] reference chronology is that the ARM cyclostratigraphy is carried by depositional magnetite, while the magnetostratigraphy is carried, in some parts of the section, by secondary iron sulfides. However, the time lag in iron sulfide formation cannot explain the magnitude of the offset. To fully account for the observed offset between the ARM chronostratigraphy and Gradstein et al.'s reference chronology would require the reduction diagenesis that formed the secondary iron sulfides occurred at least 20 m, and as great as 160 m, deep in the sediment column based on the sediment accumulation rates determined for the Arguis (Figure 9). Reduction diagenesis is observed to occur within the top meter or two of the sediment column and with time offsets of 10^4 years rather than 10^5 years [*Karlin*, 1990; *Tarduno*, 1994; *Yamazaki et al.*, 2003]. The absolute time resolution of the ARM cyclostratigraphy is, therefore, at worst 200–400 kyr which is about 1% or less than the depositional age. This resolution is the same order of magnitude as the age

uncertainty reported by *Gradstein et al.* [2004] and *Cande and Kent* [1992, 1995]. The relative age resolution within the ARM cyclostratigraphy is higher, on the order of 50 kyr, or half an eccentricity cycle.

[52] Based on results from eccentricity tuning, accumulation rates vary from 0.05 to 0.2 m/kyr in the bottom 150–200 m of the section (Figure 9e). The accumulation rate then steadily increases up to an average rate of about 0.4 m/kyr at the top of the section with periodic spikes in accumulation rate that can be as great as 1.2 m/kyr. These spikes occur about every 400 kyr in the middle of the section (150–550 m) and can be resolved to be about 100 kyr apart in the uppermost part of the section indicating that sediment accumulation rate appears to be responding to astronomically driven global climate variations. The analyzed section represents a total of 3,645 kyr, from 36.230 Ma to 39.875 Ma. The observed increase in accumulation rate up section determined through ARM cyclostratigraphy is supported by stratigraphic changes from thin, fine-grained beds to thick, coarse-grained sand beds associated with delta progradation (Figure 2).

5.4. Magnetic Mineral Climate Encoding

[53] The ARM cyclostratigraphy of the Arguis Formation suggests climate variations are encoded by the concentration of depositional magnetite. Given the χ_{ARM}/SIRM ratios that range from 1.2 to 1.8×10^{-3} m/A arguing for a fluvial source of the magnetite, and a deltaic depositional setting for the Arguis, the most plausible mechanism for the climate control of magnetite concentration is runoff variations from the continent. This interpretation is further bolstered by the coherency analysis indicating that the eccentricity-tuned ARM cyclostratigraphy is in phase with October and November insolation for the Arguis's paleolatitude (35°N [*Besse and Courtillot*, 2002]) in the Eocene (Figure 11). A Mediterranean climate would be expected for the Arguis given its paleolatitude and location on the western coast of the continent; October–November would coincide with a Mediterranean climate's fall to winter rainy season. Runoff variations have been attributed to orbital-scale climate change at precession frequencies for regions of the Atlantic Ocean and western Europe in the Eocene [*Mayer and Appel*, 1999; *Sloan and Huber*, 2001]. To explain the concentration variations of magnetite in the marine Arguis formation, a dilution model needs to be invoked. Larger values of ARM, indicating greater concentrations of depositional magnetite, suggest an increase in terrestrial input into a background of nonmagnetic marine carbonate. The dilution model is needed since the magnetite concentration within the terrestrial component of the Arguis sediments probably remains fairly constant. The ARM variations indicate fluctuations in the ratio of marine carbonate to terrestrial material in the Arguis that vary at astronomically driven periodicities. These variations could be due to changes in carbonate content with little change in terrestrial input, changes in terrestrial input with little change in marine carbonate production, or variations of both inputs. The observation that October/November mean insolation is synchronous with ARM strongly suggests that runoff is driving changes in terrestrial input from the continent. Alternatively, variations in carbonate production could have been caused by astronomically driven changes in the strength of the summer monsoon affecting equatorial upwelling, if the Arguis was located in regions of upwelling during the Eocene. However, according to the GCM modeling of *Huber and Sloan* [2000] the subtropical highs, and hence the latitudinal zones of equatorial upwelling, were still well south of the Jaca Basin's paleolatitude (35°) in the Eocene. These results suggest that carbonate production probably remained fairly constant at astronomical time scales for the Arguis and that terrestrial input variations are the main cause of its ARM variations.

[54] The runoff variation model for the climate encoding of the ARM cyclostratigraphy supports our choice of matching ARM maxima to eccentricity maxima for tuning ARM to eccentricity. As eccentricity increases climate variations become higher amplitude hence causing larger variations in runoff. The runoff model suggests that ARM should be in phase with eccentricity variations.

6. Conclusions

[55] Periodicity observed in the ARM data series is consistent with expected Milankovitch orbital periodicities, allowing the development of a cyclostratigraphy for the Arguis Formation based on ARM intensity. The ARM cyclostratigraphy is a more objective and robust way for identifying cyclostratigraphy in marine clastic rocks than the time intensive documentation of subtle changes in lithologic grain size or the other environmental proxies commonly used. The cyclostratigraphy developed for the Arguis Formation allows a high-resolution chronostratigraphy with applications to sedimentary

and structural geology studies. The absolute age resolution of the ARM chronostratigraphy is 1% or less based on an offset of 200–400 kyr with the *Gradstein et al.* [2004] reference chronology. The offset in age between the two chronologies may be due, in part, to the uncertainty in the chron ages for this part in the Eocene. The relative age resolution within the chronology is much better, on the order of 50 kyr, or half an eccentricity cycle. A combination of rock magnetic analyses allows the identification of magnetic mineralogy in the Arguis Formation. Magnetite, pyrrhotite, and goethite contribute to the saturation remanence, while only magnetite contributes to the ARM analyzed for cyclostratigraphy. Techniques that include tying to magnetostratigraphy and tuning to eccentricity are used to refine Milankovitch frequency resolution by accounting for variable accumulation rates. Coherency analysis between the ARM cyclostratigraphy and insolation provides information about how ARM encodes global climate variations. The increase in sediment accumulation rates up section inferred from the cyclostratigraphy is consistent with the observation of coarser, thicker beds and delta progradation up section. ARM serves as a proxy for climate change by recording Milankovitch cyclicity in magnetic mineral concentration. A climatically forced mechanism, continental runoff, can explain the encoding of orbital climate change in the variability of magnetic mineral concentration.

Acknowledgments

[56] We thank C. A. Regalla, O. V. Royo, J. Greenburg, and E. Pueyo for field assistance. This study was supported by National Science Foundation grant EAR-0409077 to D. J. Anastasio, K. P. Kodama, and J. M. Pares.

References

Agrinier, P., Y. Gallet, and E. Lewin (1999), On the age calibration of the geomagnetic polarity timescale, *Geophys. J. Int.*, *137*, 81–90, doi:10.1046/j.1365-246x.1999.00755.x.

Anastasio, D. J. (1992), Structural evolution of the External Sierra, Spanish Pyrenees, in *The Structural Geology of Fold and Thrust Belts*, edited by S. Mitra and G. W. Fisher, pp. 239–251, Johns Hopkins Univ. Press, Baltimore, Md.

Anastasio, D. J., and J. E. Holl (2001), Transverse fold evolution in the External Sierra, southern Pyrenees, Spain, *J. Struct. Geol.*, *23*, 379–392, doi:10.1016/S0191-8141(00)00102-4.

Berger, A. L., J. Imbrie, J. Hays, G. Kukla, and B. Saltzman (1984), *Milankovitch and Climate*, part 1, D. Reidel, Dordrecht, Netherlands.

Berger, A., M. Ercegovac, and F. Mesinger (2005), *Paleoclimate and the Earth Climate System*, *Sci. Meet. Serb. Acad. Sci. Arts*, vol. 110, Belgrade.

Berggren, W. A., D. V. Kent, C. C. Swisher III, and M.-P. Aubry (1995), A revised Cenozoic geochronology and chronostratigraphy, in *Geochronology, Time Scales and Global Stratigraphic Correlations*, edited by W. A. Berggren et al., *Spec. Publ. SEPM Soc. Sediment. Geol.*, 54, 129–212.

Berner, R. A. (1972), Sulfate reduction, pyrite formation, and the oceanic sulfur budget, in *The Changing Chemistry of the Oceans*, edited by D. Dyrssen and D. Jagner, pp. 347–361, John Wiley, New York.

Berner, R. A. (1984), Sedimentary pyrite formation: An update, *Geochim. Cosmochim. Acta*, *48*, 605–615, doi:10.1016/0016-7037(84)90089-9.

Besse, J., and V. Courtillot (2002), Apparent and true polar wander and the geometry of the geomagnetic field over the last 200 Myr, *J. Geophys. Res.*, *107*(B11), 2300, doi:10.1029/2000JB000050.

Bloemendal, J., B. Lamb, and J. King (1988), Paleoenvironmental implications of rock-magnetic properties of late Quaternary sediment cores from the eastern Equatorial Atlantic, *Paleoceanography*, *3*, 61–87, doi:10.1029/PA003i001p00061.

Butler, R. F. (1992), *Paleomagnetism, Magnetic Domains to Geologic Terranes*, 319 pp., Blackwell, Boston.

Cande, S. C., and D. V. Kent (1992), A new geomagnetic polarity time scale for the Late Cretaceous and Cenozoic, *J. Geophys. Res.*, *97*, 13,917–13,951.

Cande, S. C., and D. V. Kent (1995), Revised calibration of the geomagnetic polarity timescale for the Late Cretaceous and Cenozoic, *J. Geophys. Res.*, *100*, 6093–6095, doi:10.1029/94JB03098.

Canudo, J. I. (1990), Los foraminiferos planctonicos del Paleoceno-Eocene del Prepirineo oscense en el sector de Arguis, doctoral thesis, 435 pp., Univ. de Zaragoza, Zaragoza, Spain.

Canudo, J. I., E. Molina, J. Riveline, J. Serra-Kiel, and M. Sugunza (1988), Les événements biostratigraphiques de la zone pré-pyrénéenne d'Aragon (Espagne), de l'Eocêne moyen à l'Oligocêne inférieur, *Rev. Micropaleontol.*, *31*, 15–29.

Canudo, J. I., J. Malagon, A. Melendez, H. Millan, E. Molina, and J. J. Navarro (1991), Las secuencias deposicionales del Eoceno medio y superior de las Sierras exteriors (Prepirineo meridional aragones), *Geogaceta*, *9*, 81–84.

Castelltort, S., F. Guillocheau, C. Robin, D. Rouby, T. Nalpas, F. Lafont, and R. Eschard (2003), Fold control on the stratigraphic record: A quantified sequence stratigraphic study of the Pico del Aguila anticline in the south-western Pyrenees (Spain), *Basin Res.*, *15*, 527–551, doi:10.1111/j.1365-2117.2003.00218.x.

Cleveland, W. S. (1979), Robust locally weighted regression and smoothing scatterplots, *J. Am. Stat. Assoc.*, *74*, 829–836, doi:10.2307/2286407.

d'Argenio, B., A. G. Fischer, I. Premoli Silva, H. Weissert, and V. Ferreri (2004), *Cyclostratigraphy: An Essay of Approaches and Case Histories*, *Spec. Publ. SEPM Soc. Sediment. Geol.*, 81.

de Boer, P. L., and D. G. Smith (1994), *Orbital Forcing and Cyclic Sequences*, *Spec. Publ. Int. Assoc. Sedimentol.*, 19.

dePaor, D. G., and D. J. Anastasio (1987), The External Sierra: A case history in the advance and retreat of mountains, *Natl. Geogr. Res.*, *3*, 199–209.

Egli, R. (2003), Analysis of the field dependence of remanent magnetization curves, *J. Geophys. Res.*, *108*(B2), 2081, doi:10.1029/2002JB002023.

Ellwood, B. B., C. E. Brett, and W. D. MacDonald (2007), Magnetostratigraphy susceptibility of the Upper Ordovician Kope Formation, northern Kentucky, *Palaeogeogr. Palaeoclimatol. Palaeoecol.*, *243*, 42–54, doi:10.1016/j.palaeo.2006.07.003.

Ghil, M., et al. (2002), Advanced spectral methods for climatic time series, *Rev. Geophys.*, *40*(1), 1003, doi:10.1029/2000RG000092.

Gradstein, F. M., et al. (2004), *A Geologic Time Scale 2004*, Cambridge Univ. Press, New York.

Halls, H. C. (1976), A least-squares method to find a remanence direction from converging remagnetization circles, *Geophys. J. R. Astron. Soc.*, *45*, 297–304.

Hinnov, L. A. (2000), New perspectives on orbitally forced stratigraphy, *Annu. Rev. Earth Planet. Sci.*, *28*, 419–475, doi:10.1146/annurev.earth.28.1.419.

Hinnov, L. A. (2004), Earth's orbital parameters and cycle stratigraphy, in *A Geologic Time Scale 2004*, edited by F. Gradstein, J. Ogg, and A. Smith, chap. 4, pp. 55–62, Cambridge Univ. Press, Cambridge, U. K.

Hogan, P. J. (1993), Geochronologic, tectonic, and stratigraphic evolution of the southwest Pyrenean foreland basin, northern Spain, Ph.D. dissertation, 220 pp., Univ. of South. Calif., Los Angeles.

Hogan, P. J., and D. W. Burbank (1996), Evolution of the Jaca piggyback basin and emergence of the external Sierra, southern Pyrenees, in *Tertiary Basins of Spain the Stratigraphic Record of Crustal Kinematics*, edited by P. F. Friend and C. J. Dabrio, pp. 153–160, Cambridge Univ. Press, New York.

Holl, J. E., and D. J. Anastasio (1995), Cleavage development within a foreland fold and thrust belt, southern Pyrenees, Spain, *J. Struct. Geol.*, *17*, 357–369, doi:10.1016/0191-8141(94)00062-5.

Hounslow, M. W., and B. A. Maher (1999), Source of the climate signal recorded by magnetic susceptibility variations in Indian Ocean sediments, *J. Geophys. Res.*, *104*, 5047–5061, doi:10.1029/1998JB900085.

House, M. R., and A. S. Gale (1995), *Orbital Forcing Time-Scales And Cyclostratigraphy*, *Geol. Soc. Spec. Publ.*, 85.

Huber, M., and L. C. Sloan (2000), Climatic responses to tropical sea surface temperature changes on a "greenhouse" Earth, *Paleoceanography*, *15*, 443–450, doi:10.1029/1999PA000455.

Karlin, R. (1990), Magnetite diagenesis in marine sediments from the Oregon continental margin, *J. Geophys. Res.*, *95*, 4405–4419, doi:10.1029/JB095iB04p04405.

Kirschvink, J. L. (1980), The least-squares line and plane and the analysis of paleomagnetic data, *Geophys. J. R. Astron. Soc.*, *62*, 699–718.

Kramow, A. N. (1958), *Paleomagnetism and Stratigraphic Correlation*, *Gostoptechizdat*, Saint Petersburg, Russia.

Kruiver, P. P., M. J. Dekkers, and D. Heslop (2001), Quantification of magnetic coercivity by the analysis of acquisition curves of isothermal remanent magnetization, *Earth Planet. Sci. Lett.*, *189*, 269–276, doi:10.1016/S0012-821X(01)00367-3.

Kruiver, P. P., W. Krijgsman, C. G. Langereis, and M. J. Dekkers (2002), Cyclostratigraphy and rock-magnetic investigation of the NRM signal in late Miocene palustrine-alluvial deposits of the Librilla section (SE Spain), *J. Geophys. Res.*, *107*(B12), 2334, doi:10.1029/2001JB000945.

Kumar, A. A., V. P. Rao, S. K. Patil, P. M. Kessarkar, and M. Thamban (2005), Rock magnetic records of the sediments of the eastern Arabian Sea: Evidence for late Quaternary climatic change, *Mar. Geol.*, *220*, 59–82, doi:10.1016/j.margeo.2005.06.038.

Labaume, P., M. Seguret, and C. Seyve (1985), Evolution of a turbiditic foreland basin and analogy with an accretionary prism: Example of the Eocene south-Pyrenean basin, *Tectonics*, *4*(7), 661–685, doi:10.1029/TC004i007p00661.

Larrasoaña, J. C., J. M. Pares, and E. L. Pueyo (2003), Stable Eocene magnetization carried by magnetite and iron sulphides in marine marls (Pamolona-Arguis Formation, southern Pyrenees, northern Spain), *Stud. Geophys. Geod.*, *47*, 237–254, doi:10.1023/A:1023770106613.

Laskar, J., P. Robutel, F. Joutel, M. Gastineau, A. C. M. Correia, and B. Levrard (2004), A long term numerical solution for the insolation quantities of the Earth, *Astron. Astrophys.*, *428*, 261–285, doi:10.1051/0004-6361:20041335.

Latta, D. K., D. J. Anastasio, L. A. Hinnov, M. Elrick, and K. P. Kodama (2006), Magnetic record of Milankovitch rhythms in lithologically non-cyclic marine carbonates, *Geology*, *34*(1), 29–32, doi:10.1130/G21918.1.

Lowrie, W. (1990), Identification of ferromagnetic minerals in a rock by coercivity and unblocking temperature properties, *Geophys. Res. Lett.*, *17*(2), 159–162, doi:10.1029/GL017i002p00159.

Mann, M. E., and J. M. Lees (1996), Robust estimation of background noise and signal detection in climatic time series, *Clim. Change*, *33*, 409–445, doi:10.1007/BF00142586.

Mayer, H., and E. Appel (1999), Milankovitch cyclicity and rock-magnetic signatures of paleoclimatic change in the Early Cretaceous Biancone Formation of the Southern Alps, *Italy, Cretaceous Res.*, *20*, 189–214, doi:10.1006/cres.1999.0145.

Meigs, A. J. (1997), Sequential development of selected Pyrenean thrust faults, *J. Struct. Geol.*, *19*, 481–502, doi:10.1016/S0191-8141(96)00096-X.

Millan, H., M. Aurell, and A. Melendez (1994), Synchronous detachment folds and coeval sedimentation in the Pre-pyrenean External Sierras (Spain): A case study for a tectonic origin of sequences and system tracts, *Sedimentology*, *41*, 1001–1024, doi:10.1111/j.1365-3091.1994.tb01437.x.

Moskowitz, B. M., R. B. Frankel, and D. A. Bazylinski (1993), Rock magnetic criteria for the detection of biogenic magnetite, *Earth Planet. Sci. Lett.*, *120*, 283–300, doi:10.1016/0012-821X(93)90245-5.

Mutti, E., M. Seguret, and M. Sgavetti (1988), Sedimentation and deformation in the Tertiary sequences of the southern Pyrenees, *Mediter. Basins Conf. Field Trip 7*, 153 pp., Am. Assoc. of Pet. Geol., Tulsa, Okla.

Newton, M. L. (2006), Rock magnetic cyclostratigraphy, orbital forcing, and high-resolution age constraints from an Eocene marine flysch, Spanish Pyrenees, Masters thesis, 109 pp., Lehigh Univ., Bethlehem, Pa.

Oldfield, F., A. Hunt, M. D. H. Jones, R. Chester, J. A. Deargin, L. Olsson, and J. M. Prospero (1985), Magnetic differentiation of atmospheric dusts, *Nature*, *317*, 516–518, doi:10.1038/317516a0.

Olsen, P. E., and J. H. Whiteside (2008), Pre-Quaternary Milankovitch cycles and climate variability, in *Encyclopedia of Paleoclimatology and Ancient Environments*, edited by V. Gornitz, pp. 826–835, Kluwer Acad., Dordrecht, Netherlands.

O'Reilly, W. (1984), *Rock and Mineral Magnetism*, 220 pp., Blackie, Glasgow.

Paillard, D., L. Labeyrie, and P. Yiou (1996), Macintosh program performs time-series analysis, *Eos Trans. AGU*, *77*, 379, doi:10.1029/96EO00259.

Pälike, H., N. J. Shackleton, and U. Rohl (2001), Astronomical forcing in Late Eocene marine sediments, *Earth Planet. Sci. Lett.*, *193*, 589–602, doi:10.1016/S0012-821X(01)00501-5.

Pares, J. M., K. P. Kodama, D. J. Anastasio, and M. L. Newton (2006), Magnetic reversal stratigraphy of Eocene growth strata, South Pyrenean fold-and-thrust belt, *Eos Trans. AGU*, *87*(36), Jt. Assem. Suppl., Abstract GP41B-03.

Peters, C., and M. J. Dekkers (2003), Selected room temperature magnetic parameters as a function of mineralogy, concentration and grain size, *Phys. Chem. Earth*, *28*, 659–667.

Pickering, K. T., and N. J. Bayliss (2009), Deconvolving tectono-climatic signals in deep-marine siliciclastics, Eocene Ainsa basin, Spanish Pyrenees: Seesaw tectonics versus eustasy, *Geology*, *37*, 203–206, doi:10.1130/G25261A.1.

Pueyo, E. L. (2000), Rotaciones paleomagnéticas en sistemas de pliegues y cabalgamientos: Tipos, causas, siginificado y aplicaciones (ejemplos de las Sierras Exteriores y Cuenca de Jaca, Pirineo Aragonés), Ph.D. thesis, 296 pp., Univ. de Zaragoza, Zaragoza, Spain.

Pueyo, E. L., H. Millán, and A. Pocovî (2002), Rotation velocity of a thrust: A paleomagnetic study in the External Sierras (southern Pyrenees), *Sediment. Geol.*, *146*, 191–208, doi:10.1016/S0037-0738(01)00172-5.

Puigdefabregas, C. (1975), *La Sedimentation Molasica en la Cuenca de Jaca*, *Monogr.* 104, Inst. de Estud. Pirenaicos, Jaca, Spain.

Rodriguez-Pintó, A., E. L. Pueyo, A. Pocoví, A. Barnolas, J. M. Samsó, and I. Gil-Peña (2006), Datos magnetoestratigráficos prelinares de series Luteciense-Cuisienses en el frente pirenaico meridional occidental, paper presented at Magiber IV, Univ. de Vigo, Vigo, Spain, 28–29 Sept.

Roest, W. R., and S. P. Srivastava (1991), Kinematics of the plate boundaries between Eurasia, Iberia, and Africa in the North Atlantic from Late Cretaceous to present, *Geology*, *19*, 613–616, doi:10.1130/0091-7613(1991)019<0613:KOTPBB>2.3.CO;2.

Schaub, H. (1981), Nummulites et Assilines de la Tethys paleogene, taxinomie, phylogenie et biostratigraphie avec deux volumes d'atlas, *Mem. Suisses Paleontol.*, *104–106*, 1–238.

Serra-Kiel, J., et al. (1998), Tethyan Paleocene-Eocene larger foraminifera biostratigraphy: Shallow benthic zones, in *International Symposium on Foraminifera, Forams '98: Proceedings of the Meeting and Abstracts With Programs*, edited by J. Longoria and M. Gamper, pp. 97–98, Soc. Mex. de Paleontol., Monterrey, Mexico.

Serra-Kiel, J., C. Ferràndez-Canadel, L. Cabrera, M. Marzo, P. Busquets, F. Colombo, and S. Reguant (2003), Discusión and replan: Basin infill architecture and evolution from magnetostratigraphic cross-basin correlations in the southeastern Pyrenean foreland basin, *Geol. Soc. Am. Bull.*, *115*, 249–252, doi:10.1130/0016-7606(2003)115<0249:DARBIA>2.0.CO;2.

Shackleton, N. J., I. N. McCave, and G. P. Weedon (1999a), Astronomical (Milankovitch) calibration of the geological time-scale: A discussion, *Philos. Trans. R. Soc. London, Ser. A*, *357*, 1731–2007.

Shackleton, N. J., S. J. Crowhurst, G. P. Weedon, and J. Laskar (1999b), Astronomical calibration of Oligocene-Miocene time, *Philos. Trans. R. Soc. London, Ser. B*, *357*, 1907–1929.

Sloan, L. C., and M. Huber (2001), Eocene oceanic responses to orbital forcing on precessional time scales, *Paleoceanography*, *16*(1), 101–111, doi:10.1029/1999PA000491.

Sztrákos, K., and S. Castelltort (2001), La sédimentologie et les foraminifères bartoniens et priaboniens des coupes d'Arguis (Preépyrénées aragonaises, Espagne). Incidence sur la corrélation des biozones à la limite Bartonien/Priabonien, *Rev. Micropaleontol.*, *44*, 233–248.

Taner, M. T. (2000), Attributes revisited, technical publication, Rock Solid Images, Inc., Houston, Tex. (Available at http://www.rocksolidimages.com/pdf/attrib_revisited.htm)

Tarduno, J. A. (1994), Temporal trends of magnetic dissolution in the pelagic realm: Gauging paleoproductivity?, *Earth Planet. Sci. Lett.*, *144*, 315–326, doi:10.1016/0012-821X(94)90255-0.

Wei, W. (1995), Revised age calibration points for the geomagnetic polarity time scale, *Geophys. Res. Lett.*, *22*, 957–960, doi:10.1029/95GL00377.

Yamazaki, T., A. L. Abdeldayem, and K. Ikehara (2003), Rock-magnetic changes with reduction diagenesis in Japan Sea sediments and preservation of geomagnetic secular variation in inclination during the last 30,000 years, *Earth Planets Space*, *55*, 327–340.

Zhang, W., Y. Xing, L. Yu, H. Feng, and M. Lu (2008), Distinguishing sediments from the Yangzte and Yellow Rivers, China: Mineral magnetic approach, *Holocene*, *18*, 11391145, doi:10.1177/0959683608095582.

Zijderveld, J. D. A. (1967), A.C. demagnetization of rocks: Analysis of results, in *Methods in Paleomagnetism*, edited by D. W. Collinson, K. M. Creer, and S. K. Runcorn, pp. 254–286, Elsevier, Amsterdam.